

1 **TCSEIS-1D: An Interactive 1D Code for temperature and**
2 **composition modelling of the crust and mantle from seismological**
3 **data**

4
5 Mariano S. Arnaiz-Rodríguez ^{1*,2}, Javier Fullea ^{1,3}

6 ¹ Department of Physics of the Earth and Astrophysics, Universidad Complutense de Madrid (UCM), Madrid 28040,
7 Spain.

8 ² Institut de Physique du Globe de Paris, Université de Paris UMR 7154, CNRS, F-75005 Paris, France

9 ³ Geophysics section, Dublin Institute for Advanced Studies, Dublin, Ireland

10 *Correspondence to:* Mariano S. Arnaiz-Rodríguez (mararnai@ucm.es)

11 Contact: Mariano S. Arnaiz-Rodríguez (mararnai@ucm.es)

12 **Abstract:** We present TCSEIS-1D, a software to model the Earth's thermochemical and geophysical structure from the
13 surface down to the core-mantle boundary (CMB). The code is designed to estimate geophysical parameters of the Earth's
14 crust and mantle from petrological and thermal information within a thermodynamically consistent framework and to
15 perform forward 1D coupled geophysical-petrological modelling of the structure of the Earth. Developed in Julia
16 Language, the open-source code is intended to be an easy-to-use, flexible, and fast. TCSEIS-1D includes tools to exploit
17 the large repertoire of 1D seismological data available, namely: surface wave dispersion curves (of fundamental and
18 higher modes of Rayleigh and Love waves) and receiver functions (of P, S, and SKS waves). Surface heat flow and
19 isostatic topography can also be modelled. Four simple examples that illustrate the capabilities of the code are presented
20 to show the sensitivity of Rayleigh wave phase velocity curves and P-to-S receiver functions to compositional and
21 temperature variations.

Formatted: French

Formatted: Spanish

Formatted: Spanish

Formatted: Spanish

Formatted: Spanish

Formatted: English (US)

31

32 1 Introduction

33 The interpretation of geophysical data is a complex process that involves the quantitative treatment of measurements in
34 order to retrieve information (presented as models or images) describing the Earth's inner structure (e.g., Aki et al., 1977;
35 Dziewonski and Anderson, 1981; Telford et al., 1990; Grand, 2002; Rawlinson and Sambridge, 2003; Shapiro et al.,
36 2005; Schaeffer and Lebedev, 2013; Fullea et al., 2021). The complexity and reliability of any geophysical model depend
37 extensively on the nature (and quality) of the data selected for its characterization (e.g., Mosegaard & Tarantola, 1997;
38 Bosch, 1999). For example, single-station P-to-S receiver functions analysis can be used to infer the depth of the Moho
39 discontinuity and the average V_p/V_s relationship for all the crust (e.g., Zhu and Kanamori, 2000; Niu and James, 2002),
40 while surface wave dispersion measurements are suitable to image the shear-wave velocity structure of a region via
41 inversion (e.g., Brune and Dorman, 1963; Yanovskaya et al., 1998; Priestley and McKenzie, 2006; Lebedev et al., 2009).
42 Each one of these examples is largely limited by the sensitivity, resolution, and noise inherent to every individual data
43 type. Receiver functions are sensitive to the depth of sharp acoustic interfaces (but can only resolve velocity contrast and
44 not absolute velocities), whereas surface waves are sensitive to shear wave velocity gradients (with comparatively smaller
45 sensitivity to interfaces, e.g., Julià et al., 2000). In order to overcome their individual limitations, both receiver functions
46 and surface waves can be jointly inverted or modeled to study the lithospheric structure under a single seismological
47 station (e.g., Julià et al., 2000; Tkalčić et al., 2012; Calò et al., 2016; Levin et al., 2023).

48 The integration of different data sets generally requires relationships between all the quantitative variables (physical
49 properties) involved in the various forward problems. On the one hand, some of them can be relatively easily connected,
50 like crustal compressional wave velocity (V_p) and density (ρ), for which several empirical formulas exist based on
51 extensive data bases (e.g., Ludwig et al., 1970; Christensen and Mooney, 1995; Godfrey et al., 1997; Brocher, 2005). On
52 the other hand, other parameters like attenuation (Q_p , Q_s) or the relationship between shear wave velocity (V_s) and
53 density (ρ) are comparatively more difficult to correlate. Although it is tempting to assume that all properties can be
54 correlated by simple equations (e.g. a simple polynomial formulation c.f. Bosch (1999)) or that some may be discarded
55 (e.g., the assumption of elastic wave propagation), the reality is that it is more accurate to describe them with a probability
56 density function within an integrated framework.

57 One effective approach to overcoming this issue is to estimate the required parameters directly from the
58 petrological composition and the in-situ temperature and pressure conditions. For instance, density (ρ) and wave speeds
59 (V_p and V_s) can be estimated from the rock's composition (\mathcal{C}), temperature (\mathcal{T}) and pressure (\mathcal{P}). Furthermore, as
60 porosity and fluids can have a strong effect on these values at upper crustal levels corrections must be applied (e.g., Athy,
61 1930). Therefore, instead of trying to "guess" what an appropriate value for one master property would be, and then
62 compute all others in relation to it (e.g., Jacobsen et al., 2008; Arnaiz-Rodríguez et al., 2021), it is more advantageous
63 and consistent to estimate all parameters directly from the Temperature-Pressure-Rock Composition triad ($\mathcal{T}\mathcal{P}\mathcal{C}$). In this
64 way, we turn the "plural geophysical data" problem into the "lithology estimation" one, as named by Bosch (1999). The
65 integrated geophysical-petrological strategy, as shown by many previous works (e.g., Afonso et al., 2008; Fullea et al.,
66 2009; Khan et al., 2009; Munch et al., 2018; Bissig et al., 2021; Munch et al., 2021; Fullea et al., 2021), yields
67 thermochemical results more straightforwardly interpreted into geological terms than classical —purely geophysical—
68 approaches. Here, we present TCSEIS-1D (Temperature and Composition SEIsmological-1D), a simple forward code to
69 model the thermal and compositional structure of the crust and mantle down to the core-mantle boundary (CMB) primarily
70 from seismological data, i.e., Rayleigh and Love dispersion curves (group and phase velocity curves) and several types
71 of elastic and isotropic receiver functions (the standard P-to-S as well as S-to-P and SKS-to-P). Available codes

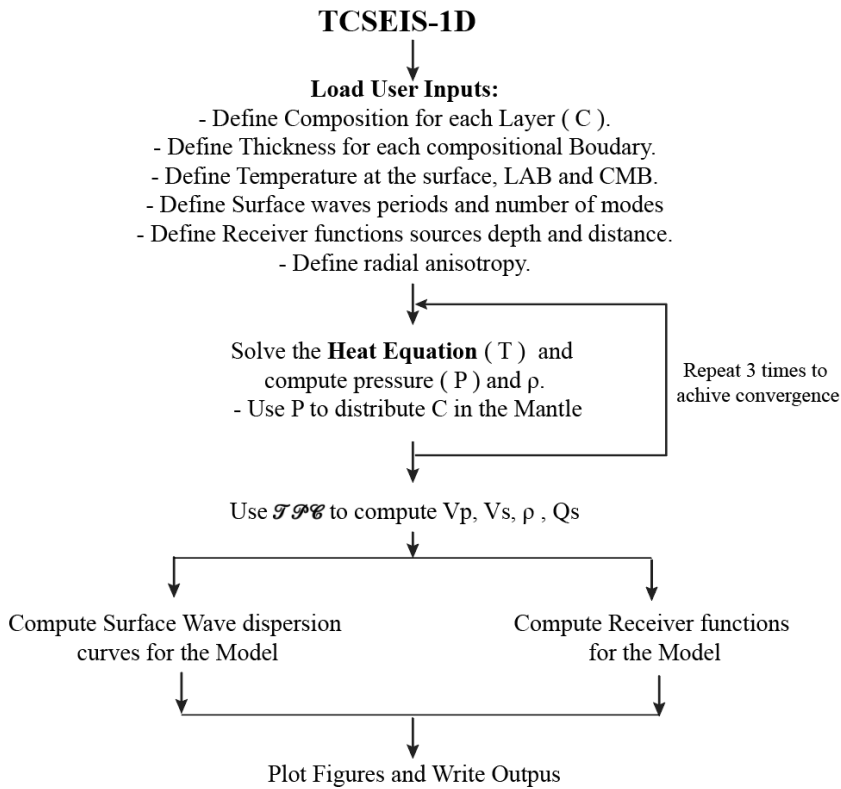
72 implementing an integrated geophysical-petrological modelling approach (either forward modelling or inversion) are
73 mostly restricted to the lithosphere/upper mantle and do not include a lithological parametrization of the crust (e.g.,
74 Afonso et al., 2008, Fullea et al., 2009, Afonso et al., 2013a,b; Fullea et al., 2021).
75 TCSEIS-1D is implemented in Julia Language (Bezanson et al., 2017) for diverse reasons: it is widely used in the
76 scientific community, flexible, open source, efficient, and has cross-platform compatibility, among others. Although Julia
77 is still considered the "new" scientific language, it is actively used in geodesy, geostatistics, and seismology (e.g., Joshua
78 et al., 2020; Xu et al., 2020; Zhu et al., 2022), and it is rapidly spreading across different disciplines (e.g., Dinari et al.,
79 2019; Gao et al., 2020). Among its most notable features are: i) fast execution time (generally approaching C or Fortran-
80 like performance); ii) dynamic typing, debugging, and syntax correction (much like Matlab or Python); iii)
81 interoperability (it makes it easy to integrate codes from C, Python, Fortran, R, Matlab, etc.); iv) geared toward scientific
82 computing; multiple dispatch (multiple methods in the same function for different input arguments); v) powerful parallel
83 computing and GPU capabilities.

84 TCSEIS-1D can be employed to: (a) test geophysical models in the *JPC* model space; (b) estimate a possible
85 solution to the composition and thermal structure of the Earth's main layers (limited by the resolution, quality, and
86 sensitivity of the input data), (c) link velocities and density variations to *JPC* variations. After introducing the equations
87 and assumptions that drive TCSEIS-1D's engine, the general framework of the code is presented, as well as the validation
88 (against other codes) of the different sections that make up the software package. Finally, a few examples are presented
89 to showcase the functionality and applicability of TCSEIS-1D with a suggestion of additional work for future versions.

90 A general flowchart of the current version of TCSEIS-1D is provided in Fig 1.

Formatted: English (US)

Formatted: English (US)



93
94
95
96
97
98
99
100
101
102
103
104
105
106
107
108
109
110

Figure. 1. TCSEIS Flowchart.

Formatted: English (US)

2 Methods and Considerations

Mechanical properties of rocks, specifically compressional wave-speed (V_p), shear wave-speed (V_s), and density (ρ), vary in a wide range. Even though there are some clear trends in their behaviour (e.g., sedimentary rocks tend to have lower density than igneous rocks; or mafic rocks have higher V_p than felsic rocks; e.g. Telford et al 1990; Brocher, 2005), a large degree of overlap exists. For example, a crustal rock with $V_p=6.05$ km/s can represent a very old and consolidated carbonatic rock (i.e., a dolomite) or a felsic rock rich in quartz (i.e., a greisen). The consideration of metamorphic rocks affected by, for example, metastability (i.e., departure from thermodynamic equilibrium) makes this statement even more complex, as these rocks tend to show properties different than those associated with its protoliths (e.g., Telford et al., 1990).

Seismic velocities and density of Earth's rocks depend on several parameters, namely: temperature, pressure, mineral composition, melt fraction, fluids, and, in the case of crustal rocks, porosity and pore fluids (e.g., Christensen and Mooney, 1995; Brocher, 2005). This complex mixture yields the perfect recipe for the overlap of geophysical parameter values for different rock types and geological settings as usually reported (e.g., Telford et al., 1990; Brocher, 2005). For

111 our purpose of modeling geophysical data using petrological and thermal parameters, it is cardinal to reduce the number
112 of free variables while keeping, at the same time, a flexible enough parameterization to represent the Earth's complexity.
113 In this study, for the crust, we chose several ternary diagrams to classify igneous and sedimentary rocks based on
114 mineralogical composition (Streckeisen, 1974; Le Bas and Streckeisen, 1991; Philpotts and Jay, 2009; Bissell, 2021). By
115 contrast, in the mantle, we adopt two major oxides (Al₂O₃ and FeO) as independent variables and compute the other
116 CFMAS oxides (CaO, FeO, MgO, Al₂O₃, and SiO₂) from statistical correlations based on global mantle xenoliths and
117 peridotite massifs data bases (e.g., Afonso et al., 2013 a,b; Fullea et al., 2021).

118 2.1 The geotherm.

119 In general, temperature increases with depth (z) within the Earth. Heat transport inside the Earth is mainly a 3D problem
120 in which the mantle is in convection at a high Rayleigh number ($Ra > 10^7$; e.g., Ricard, 2007), bringing heat from the
121 Core-Mantle Boundary, where the D'' layer acts as the lower hot thermal boundary of the convection, up to the base of
122 the thermal lithosphere, the Lithosphere-Asthenosphere-Boundary (LAB). The LAB (usually defined by the 1250–1330
123 °C isotherm; e.g., Grose and Afonso, 2019; Ball et al., 2021; Audhkhasi and Singh, 2022) represents the base of the
124 portion of the upper mantle where viscosity is high enough ($>10^{23}$ Pa s, e.g., Nakada, 1996) to prevent mantle convection,
125 leaving conduction as the dominant heat transport process (e.g., Turcotte et al., 2007). The lithospheric geotherm controls
126 the surface heat flow, which is an output of TCSEIS-1D.

127 Here we are interested in a parametrization that reflects the temperature domain division between the lithosphere and the
128 sublithospheric (upper and lower) mantle, ensuring energy budget consistency across the two domains and being flexible
129 enough to model transient and steady-state thermal situations. The geotherm in TCSEIS-1D follows a 1D thermal
130 parametrization, where the temperature varies only with depth (z):

$$132 \rho(z)Cp(z) \frac{dT}{dt} = \frac{\partial}{\partial z} (k(z,T) \frac{\partial T}{\partial z}) + Hr(z) \quad (\text{Eq. 1})$$

133 where $\rho(z)$ is the density, $Cp(z)$ is the heat capacity, $k(z,T)$ is the thermal conductivity, and $Hr(z)$ is the radiogenic heat
134 production as a functions of depth (e.g., Gerya, 2007).

135 We solve Eq. 1 on an equispaced 1-km vertical grid using the Finite Differences technique with the following initial and
136 boundary conditions:

- 137 - The temperature at the surface of the Earth is constant (and defined by the user).
- 138 - The temperature at the CMB is constant (and defined by the user).
- 139 - The LAB depth and temperature (e.g., 200 km and 1573 K) are defined by the user and are set as an inner boundary
140 condition to the solution of Eq.1. This point is fixed in the solution (unless a collocated thermal anomaly is input by
141 the user) and, therefore, it divides the temperature field into two domains: from the surface to the LAB (conductive
142 geotherm, typically 5-25 K/km), and from the LAB to the CMB (convective geotherm, typically 0.25-0.6 K/km).
- 143 - The asthenospheric (or sublithospheric mantle, depth $>$ LAB depth), the transitional mantle (or transition zone, i.e.,
144 from 410 km to 660 km depth), and the lower mantle (depth $>$ 660 km) geotherms are defined by two initial temperature
145 gradients provided by the user (by default, 0.45 K/km in the asthenosphere and transition zone, and 0.25 K/km in the
146 lower mantle). Therefore, below the lithosphere, a pseudo-convective geotherm is calculated, solving Eq. 1 for the
147 initial conditions from the thermal gradients. In this way, we parametrize a continuous temperature gradient in the
148 thermal buffer immediately below the lithosphere where both conduction and convective processes are expected.
- 149 - The time variable in Eq. 1 is, in general, taken large enough to reach thermal steady-state conditions. Transient thermal
150 scenarios in the lithosphere can be modeled by adding the appropriate time input.
- 151

152 - Vertical variations in radiogenic heat production, thermal conductivity, and heat capacity are considered in the
153 temperature modeling within TCSEIS-1D. The thermal conductivity of mantle rocks is computed according to the
154 equation and parameters proposed by Hofmeister (1999) as a function of temperature, pressure, and predominant
155 mineral type. In this work, we assume one representative mineral chosen from the pyrolite compositional model (e.g.,
156 Ringwood, 1982; Irifune and Isshiki, 1998; Irifune et al., 2010; Hirose, 2006) for each mantle section in order to
157 compute thermal conductivity: olivine (lithosphere and asthenosphere), ringwoodite (upper transition zone, from ~410
158 km to ~550 km), wadsleyite (lower transition zone, from ~550 km to ~660 km), and bridgmanite (lower mantle; e.g.,
159 Hamblin and Christiansen, 2004; Lin et al., 2013). The code also offers the possibility of adding thermal anomalies
160 with respect to the conductive (lithosphere) and pseudo-convective geotherm (asthenosphere, transition zone, and
161 lower mantle) computed as described above by setting a depth range and a temperature anomaly.

162
163 Eq. 1 can model the geotherm in a variety of tectonic and geodynamic settings, for example: (a) continental and mature
164 oceanic lithosphere in thermal steady state; (b) Mid Oceanic Ridges and young oceanic lithosphere in transient thermal
165 state; and (c) close to the adiabatic geothermal gradient below the lithosphere with the typical steep increase in
166 temperature observed in the vicinity of the CMB.

167
168 Note that we do not intend to solve a full geodynamic problem in the sublithospheric mantle (i.e., incorporating mantle
169 flow and dynamic topography); instead, we aim for a flexible 1D parameterization able to describe variations in the
170 geothermal gradient or temperature anomalies with respect to the reference geothermal gradients (e.g., plumes or slabs;
171 see Section 4.2 for an example) as imaged by seismic data.

172 173 **2.2 Compositional model space**

174 To simplify the existing plethora of mineral aggregates (rocks), we have split the model compositional space (\mathcal{C}) into
175 three major categories: sedimentary rocks, igneous rocks, and mantle rocks. Out of these, only igneous rocks are further
176 separated into three compositional subcategories: felsic, mafic, and ultramafic rocks (after standard geologic
177 classification, e.g., Streckeisen, 1974). In this section, we describe how each rock type is parametrized and how the
178 relevant geophysical parameters are computed from the JPC triad. Metamorphic rocks have been left out of our model
179 parametrization as their mineralogy tends to be complex, as well as some physical features that require complex numerical
180 representation (e.g., distinctive and pronounced planes of weakness). Furthermore, their classification is usually based on
181 texture and not composition, which makes it difficult to relate to our proposed parametrization. Therefore, we favor the
182 use of their protoliths, which are much simpler to describe in terms of their mineral composition and properties. For
183 example, a marble, composed of recrystallized carbonatitic minerals, can be represented as a 0% porosity carbonate. This
184 is a novel scheme as no rigorous thermochemical/lithological parametrization has been presented in previous tools
185 designed for integrated modelling of the lithosphere (e.g., Afonso et al., 2008, 2013a, b; Fullea et al., 2009, 2021).

186 187 **2.2.1 Sedimentary Rocks**

188 In TCSEIS-1D the sedimentary compositional space (\mathcal{C}) is discretized following the simplest ternary diagram
189 provided by Bissell (2021). Based on it, each corner of the ternary diagram stands for:

- 190 - α -Quartz (Qz).
191 - Carbonates: represented in our model by pure calcite (CaCO_3) as it is much more common than dolomite
192 ($\text{CaMg}(\text{CO}_3)_2$)

193 - Clay Minerals ($[Al, Fe]_2O_3$): representing a *mélange à parts égales* (from here onwards, mape) of three commonly
194 occurring clay minerals: Montmorillonite + Kaolinite + Illite.

195 We use the code MinVel (Hacker et al., 2004; Abers et al., 2016; Sowers et al., 2019), an extensive database of physical
196 properties of minerals from laboratory measurements (Haker et al., 2004), to estimate V_p , V_s , and ρ for all the
197 compositional space (\mathcal{C}), defined by the possible combinations of the minerals (3 values that add up to 100%, e.g., 60 %
198 quartz + 20% carbonates + 20 % clays) every 10%, for different temperatures (between 200 and 1000 K every 100 K)
199 and pressures (between 0 and 0.6 GPa every 0.025 GPa). This sampling yields three multidimensional grids (one for each
200 property) in which rock properties are stored for a range of \mathcal{TPC} values. These are linearly interpolated and saved into
201 easy-to-call Julia functions. In this way, we can estimate V_p , V_s and ρ for a fully consolidated sedimentary unit from any
202 given \mathcal{TPC} values (compositions are limited to triads consisting of multiples of 10 to guarantee numerical precision and
203 computational speed). Fig. 2 presents several examples of the geophysical properties in ternary diagrams. Notice that
204 carbonatic rocks tend to show larger velocity and density values than other lithologies, regardless of temperature, pressure
205 conditions, or porosity, and clays show the largest variations.

Formatted: English (US)

206

207 2.2.2 Crustal Igneous Rocks

208 For crustal igneous rocks, we use a similar approach to that presented for sedimentary rocks in the previous section,
209 including the use of mape where required and linear interpolation. In this case, three compositional subspaces are
210 considered, one for each igneous rock subcategory: felsic, mafic and ultramafic rocks (as defined by Streckeisen, 1974;
211 Le Bas and Streckeisen, 1991; Philpotts and Jay, 2009). We treat each subcategory as follows:

- 212 - Felsic rocks are defined in a ternary space outlined by the QAP diagram (quartz, K-feldspars, and plagioclase). We
213 discard the standard QAFP classification (quartz, K-feldspars, feldesphatoids, and plagioclase) in favor of a 3-mineral
214 space as feldspathoids (F) resemble feldspars (K), and rocks with high concentrations of F are comparatively much
215 less common. Hence, felsic rocks are defined by the ternary of: α -quartz or β -quartz (as we account for the reversible
216 change at 573 °C, which drastically impacts the determination of V_p , V_s , and ρ ; Abers and Hacker, 2016); K-feldspars
217 (a mape of Orthoclase + Sanidine); and Plagioclase (a mape of High Albite + Low Albite + Anorthite).
- 218 - Mafic rocks are considered aggregates of: anorthosite (mape of Anorthite+High Albite+Low Albite), clinopyroxene
219 (mape of Diopside+Hedenbergite) and orthopyroxene (mape of Enstatite+Ferrosilite).
- 220 - Ultramafic rocks are defined as a combination of olivine (mape of Forsterite+Fayalite), clinopyroxene (mape of
221 Diopside+Hedenbergite) and orthopyroxene (mape of Enstatite+Ferrosilite).

222

223 As with sedimentary rocks, we sample each compositional space with MinVel (Hacker et al., 2004; Abers et al., 2016;
224 Sowers et al., 2019) at variations in composition every 10% for different crustal temperatures (between 0 and 1600 K
225 every 100 K) and pressures (between 0 and 4 GPa every 0.05 GPa) and then save all results into Julia functions. In order
226 to show the variations of the V_p , V_s , and ρ values in a ternary diagram, Fig. 2 presents several examples.

Formatted: English (US)

227

Formatted: English (US)

228 Typical igneous rocks have very low primary porosity (e.g., 0.05%–0.90% for granite and 0.6–1.3 for basalts, Wiczysty,
229 1982) when compared to sediments (e.g., a typical sandstone has a porosity ranging from 10% to 40%) and are usually
230 found at high \mathcal{P} in the crust. Furthermore, even though crustal rocks are well known to have secondary porosity (e.g. high
231 density faulting), there is no simple way to account for it in V_p, V_s or ρ . Therefore, we choose not to apply any porosity
232 corrections for igneous rocks in TCSEIS-1D.

233

234

235 **2.2.3 Porosity**

236 Crustal rocks are not perfect aggregates of minerals, and their behavior is not completely elastic in some cases. Rocks (in
237 our case igneous and sedimentary) are generally porous, including secondary porosity and fractures, and hence we correct
238 their geophysical properties by the percentage of porosity (φ). Velocities (V_x) are corrected in accordance with Raymer's
239 equations (Raymer et al., 1980), while density (ρ) is corrected following Athys's law (Athys, 1930):

240

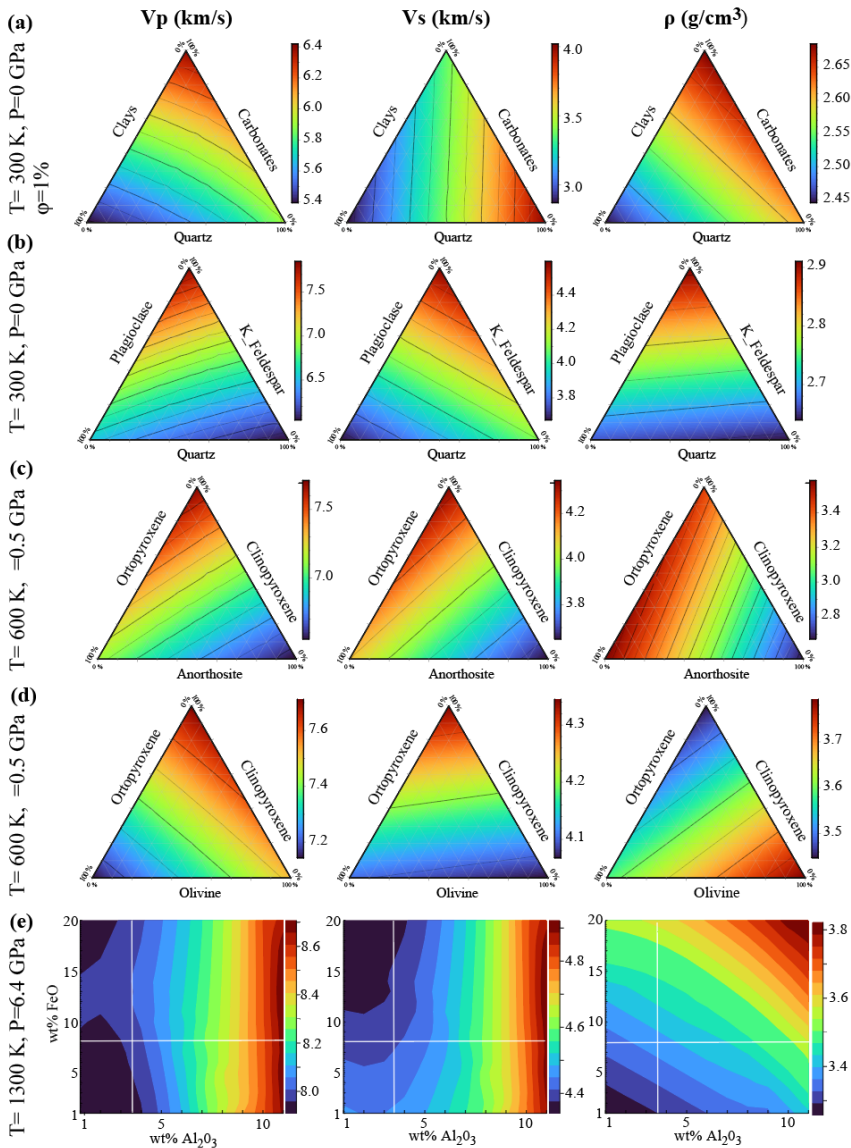
241
$$V_{rock} = (1 - \varphi/100)^2 V_{solid} + (\varphi/100) V_{liquid} \text{ (Eq. 2)}$$

242
$$\rho_{rock} = (\varphi/100 - 1) \rho_{solid} \text{ (Eq. 3)}$$

243

244 Where X_{rock} refers to the corrected property, X_{solid} to the property of the fully consolidated rock and X_{liquid} to property of
245 the fluid inside the porous scape. The user must input X_{liquid} of the fluid inside the porous space, if not the corrections are
246 applied by default as if the rocks were filled with air.

247



248
249

250 Figure 2: Examples of compressional wavespeed (V_p), shear wavespeed (V_s) and density (ρ) variations for: (a) sedimentary,
 251 igneous felsic, (c) igneous mafic, (d) igneous ultramafic and (e) mantle rocks as a function of temperature (T), pressure (P),
 252 composition and porosity (for sedimentary rocks). All color scales are similar for ease of comparison. In sedimentary rocks (a)
 253 carbonates have the higher V_p and ρ . For felsic rocks, with higher percentage of quartz, V_p and ρ becomes higher, while V_s
 254 becomes higher with the increase of plagioclase. Also, lower values of all three properties are associated with higher percentage
 255 of *K-feldspars*. For mafic rocks, all properties increase with the percentage of anorthosite and decrease with the percentage of
 256 clinopyroxene. Unlike felsic or mafic rocks, in ultramafics, each mineral dominates the decrease of a different property. On (e)
 257 the cross marks the average mantle composition.

258

259 2.2.3 Mantle Rocks

260 Compared to the crust, the Earth's mantle petrology is less complex and can be adequately represented by the modal
261 distribution of the main mineral phases (olivine, pyroxenes, and Al-bearing phases) under the consideration of
262 thermodynamic equilibrium ($T > 500$ °C). In this work we determine stable mantle mineral assemblages using a Gibbs
263 free energy minimization scheme (Connolly, 2005, 2009). Therefore, the mantle's physical properties relevant to our
264 work (V_p , V_s and ρ) are computed on these assumptions based on the \mathcal{JPC} values. A standard characterization of mantle
265 composition is based on the main major oxides in the CFMAS system (CaO–FeO–MgO–Al₂O₃–SiO₂; e.g. Irifune, 1990;
266 Irifune and Tsuchiya, 2015). To simplify the parametrization of \mathcal{C} , here we adopt the discretization of Fullea et al. (2021)
267 where the wt% amounts Al₂O₃ and FeO oxides in the mantle layers are free variables, and CaO–MgO amounts are
268 statistically correlated to Al₂O₃ based on global petrological data bases as described in Afonso et al. (2013a). Similarly
269 to Mg# (= MgO/[MgO + FeO]), Al₂O₃ has been shown to be a strong compositional indicator and, therefore, an overall
270 proxy for mantle fertility. Mantle fertility refers to the relative enrichment of the mantle in basaltic, melt-producing
271 components, such as and thus to its potential to generate partial. In particular a fertile mantle should be rich in Al₂O₃,
272 CaO, FeO, meaning more content of clinopyroxene and garnet while a depleted mantle has residue after melt extraction
273 like harzburgitic and low Al₂O₃. In contrast, neither FeO nor SiO are correlated in general with either CaO or Al₂O₃
274 (Afonso et al. 2013a). For the petrological calculations we use `Perple_X` (Connolly, 2005, 2009) and for the lower mantle
275 the databases by Xu et al. (2008) and Stixrude & Litgow-Bertelloni (2021). We sample the wide range of \mathcal{T} (from 100 to
276 4500 K) and \mathcal{P} (from 0 to 145 GPa) found in the mantle. As for the self-consistent thermodynamic data base, in the upper
277 mantle we use the Xu et al., (2008), whereas in the transition zone and lower mantle we consider Stixrude & Litgow-
278 Bertelloni (2021). \mathcal{C} values are limited to the ranges of (1-11) wt% for Al₂O₃ and (1-20) wt% for FeO. These range of
279 compositions should be more than enough to model almost every scenario in the entire mantle as values of Al₂O₃ are
280 expected to range from 1.0 wt% to 6.0 wt% and FeO is generally considered to be around 8.0 wt% (e.g., McDonough and
281 Sun, 1995). In some special cases larger ranges might be needed, e.g., Large Low Shear Velocity Provinces in the
282 lowermost mantle (e.g., Vilella et al., 2021). In Fig. 2 we show the relevant mantle properties for several \mathcal{JP} conditions.
283 In TCSEIS-1D, there are four major mantle layers defined by their wt% amounts of Al₂O₃ and FeO:

Formatted: English (US)

- 284 1) The *lithospheric mantle* extends from the Moho down to the Lithosphere-Asthenosphere Boundary, or LAB (an input
285 depth and temperature are expected from the user as explained in Section 2.2). The thickness of this layer is user-defined
286 and does not change unless thermal anomalies are incorporated into the model.
- 287 2) The *asthenospheric (or sublithospheric) mantle* extends from the LAB down to a pressure of ~14 GPa, representing
288 the average value for the transition from olivine to wadsleyite mineral phases.
- 289 3) The *transition zone mantle* extends from a pressure of ~14 GPa to a value of ~24 GPa. The later value is the average
290 pressure for the transition from ringwoodite and majorite to perovskite and ferropericlasite, the boundary between the upper
291 and the lower mantle. Note that the transition zone includes an inner phase transition from wadsleyite to ringwoodite at
292 around 520 km depth (Rigden et al., 1991; Tian et al., 2020).
- 293 4) The *lower mantle* extends from a pressure of ~24 GPa down to the CMB (a user input).

294 While the boundaries between the first two layers (i.e., LAB depth) and the bottom of the model (i.e., CMB) are input
295 parameters, in the case of the top and bottom of the mantle transition zone, the depth depends on different mineral phase
296 transitions that cannot be predicted beforehand without performing a thermodynamic calculation based on the actual \mathcal{JPC}
297 conditions. Therefore, our approach here is to initially define those mantle layer boundaries based on standard reference
298 pressure values (~14 GPa and ~24 GPa), and subsequently relocate them automatically to the depth at which the relevant

Formatted: English (US)

299 phase transitions occur. Therefore, from a compositional point of view, the depth of the base of layer 2 and 3 is effectively
300 defined by a thermodynamic equilibrium calculation. In virtue of the thermodynamic parametrization, the velocity and
301 density jumps related to phase transitions usually associated with the 410 km, 520 km, and 660 km discontinuities will
302 arise in the model even if the composition is uniform across all four mantle layers. For example, all these discontinuities
303 still appear in the model for a constant whole mantle composition (e.g., primitive mantle composition with 3.6 wt% Al₂O₃
304 and 2O₃ 8.0 wt% FeO from McDonough and Sun, 1995). Finally, the user can also specify anomalous regions
305 (compositional anomalies) within any of the four compositional layers by setting a depth range and a chemical anomaly
306 value (e.g., -0.5 wt% Al₂O₃ and +0.2 wt% FeO).

307

308 2.2.3.1 Seismic attenuation in the mantle

309 To account for anelasticity, we follow the strategy of Dannberg et al. (2017) and extrapolate the relationships for olivine
310 at upper mantle conditions derived by Jackson and Faul (2010) to the whole mantle. Notice that this is clearly a
311 simplification of the mineralogy at the mantle scale and thus its behavior in seismic attenuation terms, but Dannberg et
312 al. (2017) proved that it yields a useful first-order approximation as the results are not very dissimilar to, for example, the
313 values reported in the PREM model. Here we adopt the parametrization by Dannberg et al. (2017) as described in
314 Appendix B.

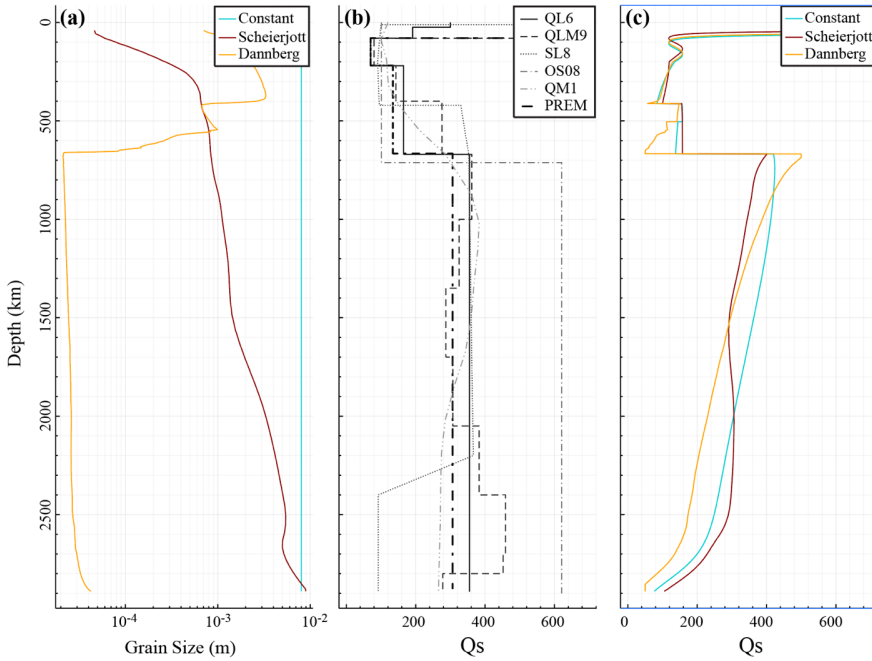
315

316 Most of the attenuation parameters are different for each major mantle mineral phase. In TCSEIS-1D, we use different
317 attenuation parameters for the most abundant mineral phases at each depth depending on their respective stability fields:
318 the upper mantle (olivine), the upper and lower transition zones (wadsleyite and ringwoodite), and the lower mantle
319 (perovskite). Grain size (d) has a large impact on the attenuation, as per our parametrization described in Appendix B. In
320 the code, the user can choose between three grain size models with depth: (a) a constant value ($d = 10$ mm), (b) the model
321 by Schierjott et al. (2020), in which d increases with depth, and (c) the model by Dannberg et al. (2017), where d decreases
322 with depth. In general terms, we find that the constant and Schierjott models fit best with the general trends of the global
323 1D models (Fig. 3).

324

Formatted: English (US)

Formatted: English (US)



325
 326
 327 **Figure 3: (a) Grain size variation with depth for the 3 models included in the code: Constant (a constant value or 10^{-2} m),**
 328 **Schierjott (the grain size variations estimated by Schierjott et al., 2020) and Dannberg (the grain size variations estimated by**
 329 **Dannberg et al., 2017). (b) Several 1D Radial models of Qs for the whole mantle: SL8 (Anderson and Hart, 1978), QM1**
 330 **(Widmer et al., 1991), QL6 (Durek and Ekstrom, 1996), QLM9 (Lawrence and Wyession, 2006), QOS08 (Oki and Shearer,**
 331 **2008), PREM (Dziewonski and Anderson, 1981). (c) Qs computed from the Burgers model of linear viscoelasticity (Jackson**
 332 **and Faul, 2010). The Constant and Schierjott models produce the closest fit the radial models.**

333 **2.2.4 Melt**

334 Accounting for melt in a 1D column requires the definition of consistent solidus and liquidus curves for the crust and the
 335 whole mantle. In the crust, we consider the equations in Gerya (2019) characterizing the solidus and liquidus temperatures
 336 for sediments and igneous rocks. In the mantle, water content and, to a lesser extent, composition control the solidus
 337 values reported in the literature (e.g., Schmidt and Poli, 1998; Hirschmann, 2000; Katz et al., 2003; Sarafian et al., 2016;
 338 Fu et al., 2018). In TCSEIS-1D, we allow the user to define the solidus curve for the upper mantle (i.e., from the Moho
 339 to a pressure of ~ 10 GPa or depth of ~ 300 km) from two sources:

- 340 - The solidus presented by Andrault et al. (2018), which corresponds to a nominally dry mantle (between 1 and 90 wt
 341 ppm),
- 342 - The second-degree polynomial by Katz et al. (2003), defined only up to 7 GPa, which corresponds to a nominally
 343 anhydrous mantle with 40–80 wt ppm of water.

344
 345 From 10 GPa to 30 GPa, we use the logarithmic anhydrous solidus curve by Herzberg et al. (2000), and from 30 GPa to
 346 120 GPa, the solidus curve by Fu et al. (2018) with ~ 400 wt ppm water can be extrapolated to the CMB conditions,
 347 according to the authors.

348 For the mantle liquidus, we use (a) a fourth-degree polynomial fitted to the liquidus curve by Litasov and Ohtani (2002),
 349 valid from 0 GPa (surface) to ~30 GPa (roughly 800 km depth), and (b) a second-degree polynomial fitting the liquidus
 350 curve by Fu et al. (2018) from 30 GPa to the CMB. With this parametrization, the solidus and liquidus curves have large
 351 jumps at the crust-mantle boundary and around 800 km, therefore we have chosen to smooth them with a rloess (Fig. 11).
 352 The volumetric melt fraction (Melt) is usually defined, for a constant pressure, as a linearly varying temperature-
 353 dependent function (e.g., Gerya and Yuen, 2003b; Burg and Gerya, 2005; Gerya, 2019; Fullea et al., 2021):

$$354 \text{Melt} = 0\% \text{ from } T \leq T_{\text{solidus}} \text{ (Eq. 4)}$$

$$355 \text{Melt} = \frac{(T - T_{\text{solidus}})}{(T_{\text{liquidus}} - T_{\text{solidus}})} 100 \text{ from } T_{\text{solidus}} < T < T_{\text{liquidus}} \text{ (Eq. 5)}$$

$$356 \text{Melt} = 100\% \text{ at } T \geq T_{\text{liquidus}} \text{ (Eq. 6)}$$

357 where T_{solidus} and T_{liquidus} are the wet solidus and dry liquidus temperatures defined by the curves described previously.
 358 Once $\text{Melt}(z)$ has been computed for each model node the associated seismic parameters (V_p , V_s , Q_s) are corrected
 359 following the experimental study by Chantel et al (2016):

$$360 V_p = 0.07\text{Melt}^2 - 0.5566\text{Melt} + 7.9235 \text{ (Eq. 7)}$$

$$361 V_s = 0.065\text{Melt}^2 - 0.5565\text{Melt} + 4.4211 \text{ (Eq. 8)}$$

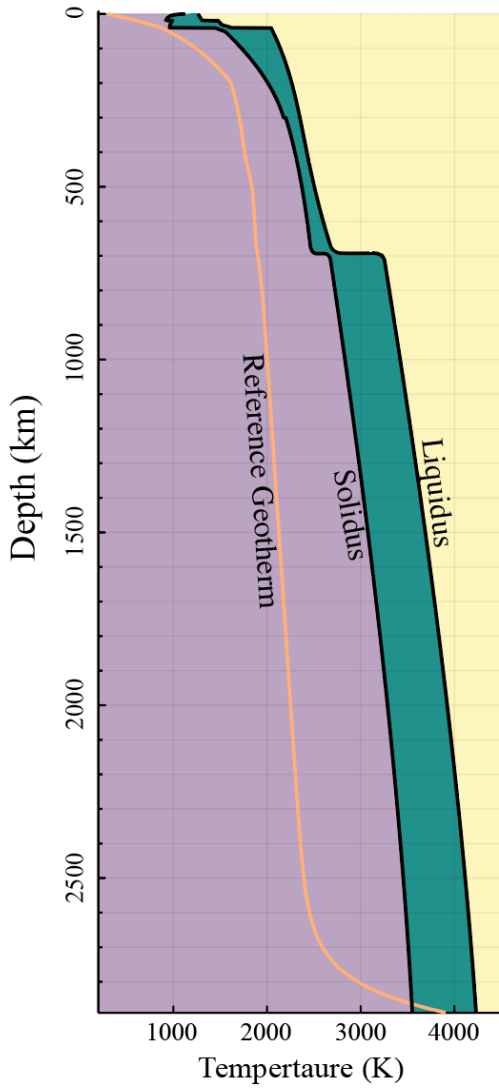
$$362 100/Q_s = 2.4063\ln(\text{Melt}) + 5.9284 \text{ (Eq. 9)}$$

363 Mantle density is corrected (becoming the effective density, ρ_{eff}) by the equation postulated by Gerya (2019):

$$364 \rho_{\text{eff}} = \rho_{\text{solid}}(1 - \text{Melt} + \text{Melt} \frac{\rho_{\text{molten}}}{\rho_{\text{solid}}}) \text{ (Eq. 110)}$$

365 where ρ_{solid} and ρ_{liquid} are the standard densities of the solid and molten rock, respectively and ρ_{solid} is the density of the
 366 solid rock at given \mathcal{TP} conditions computed as described in section 2.1 and 2.3. The values for ρ_{solid} and ρ_{liquid} are taken
 367 from the compilation of values by Gerya (2019) and could be changed by the user inside the code if required. Figure 4
 368 shows the used curves.

Formatted: English (US)



387
 388 **Figure 4: Solidus and liquidus curves from the entire crust and mantle. Solidus by: Gerya (2019), Katz et al., (2003), Herzberg**
 389 **et al (2000) and Fu et al., (2018). Liquidus by: Gerya (2019), Litasov and Ohtani (2002) and Fu et al., (2018). See text for details.**

390
 391
 392
 393

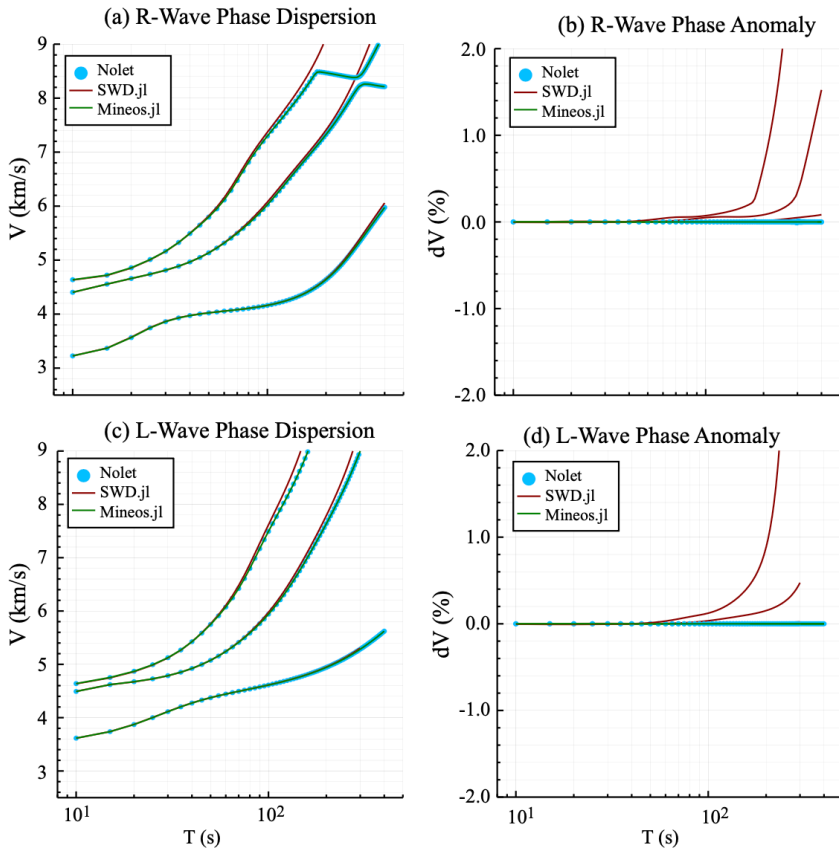
394 **2.4 Surface Wave Dispersion Forward Modeling**

395 TCSEIS-1D computes surface wave dispersion curves in two ways: from a native function SWD.jl (developed as part of
396 TCSEIS-1D) or by calling Mineos.jl, a Julia wrapper around the code Mineos developed to compute normal modes of the
397 Earth (Master et al., 2011, <https://geodynamics.org/cig>). In general terms, SWD.jl is faster than Mineos.jl, although the
398 former gives an approximated solution in contrast to the exact solution from the latter. Both run code run in CPU and the
399 computation time for a dispersion curve with 20 samples, for PREM model is in the order of 0.17 s for SWD.jl and 0.26
400 s for Mineos.jl in a Apple MacBook Air with 8 GB of RAM and and M1 chip. Also, the approximations built in SWD.jl
401 yield some high errors (>1%) in cases of very strong attenuation ($Q_s < 70$) and high-order overtone calculation.

402
403 SWD.jl is mostly based on the formulation described by Haney and Tsai (2015, 2017, 2019). These authors utilize (for
404 both Rayleigh and Love waves) a finite element approach based on the thin-layer method (Lysmer, 1970; Kausel, 2005).
405 The scheme behind SWD.jl and the corrections necessary to approximate the results from Mineos.jl are detailed in
406 Appendix A. To validate both approaches, in Fig. 5, we present a comparison between surface wave dispersion curves
407 computed by SWD.jl (the main TCSEIS-1D dispersion engine), Mineos (Masters et al., 2011) and the exact solution.
408 Each code uses a different approach for the computation: SWD.jl uses a finite element solution, whereas Mineos uses the
409 traditional normal-mode summation. Discrepancies in the results from all three codes are small in terms of phase velocity
410 ($dc < 0.045\%$) and group velocity ($dU < 0.2\%$) and might arise from the difference in the computations and/or
411 parameterization of the model for each code. For example, at $T = 50$ s, considering the PREM velocity model as input,
412 the fundamental mode Rayleigh wave phase velocity differences comparing the output of the three codes are $<0.002\%$.
413 Notice that errors increase with time because of the spherical approximation. The user can always extract the standard
414 seismic velocities and density geophysical model from the TCSEIS-1D output to perform customized seismic modeling
415 a posteriori with other tools. We recommend using Mineos.jl for modeling data with long periods ($T > 70$ s, shorter
416 periods are properly represented by SWD.jl), higher overtones (overtones 1 and 2 are well computed by SWD.jl but higher
417 overtones are not well represented in by the FEM formulation), and for studying regions with strong attenuation (as
418 SWD.jl uses and approximation to attenuation, see Appendix B for details). Note that the original Mineos code has a
419 limitation of 300 velocity layers, making it only appropriate for $T > 30$ s. On the other hand, SWD.jl is recommended for
420 shorter periods ($T < 70$ s; mainly crust and upper mantle studies) where complex models can be proposed or when
421 computational time is relevant.
422

Formatted: English (US)

Formatted: English (US)



423
424

425 **Figure 5:** Comparison between surface wave dispersion curves computed by SWD.jl (red, the main TCSEIS-1D dispersion
426 engine), Mineos (green, Masters et al., 2011) and the exact solution (blue circles marked as Nolet).

427 **2.5 Receiver Functions Forward Modeling**

428 In order to give the user a basic handling of receiver function data during the modeling stages, we have incorporated a
429 simple module (i.e., the computation is made without accounting for the effect of anisotropy or attenuation) to compute
430 synthetic receiver functions from the input geophysical model. Receiver functions are computed using a transfer function
431 between the stress and displacement known as the propagator matrix approach (Thomson, 1950; Haskell, 1953; Kennett,
432 1983). For all the receiver functions, P-to-S, S-to-P, and SKS-to-P, the sequence is similar. For each source (with a depth
433 and epicentral distance taken from the IASPI91 tables; Kennett et al., 1991), the synthetic radial and vertical components
434 (R and Z) are computed for a given 1D model and then rotated into the direction of polarization of the incident P-wave
435 (L) and its perpendicular (Q) in the R-Z plane (e.g., Vinnik, 1977; Kind et al., 1995). In general, we compute the surface
436 response in the Fourier domain for a plane impingement waveform. The transmitted impulse is assumed to arrive at the
437 surface at $t = 0$ s. Then, we calculate the time domain displacements at the surface for each direction. The computation

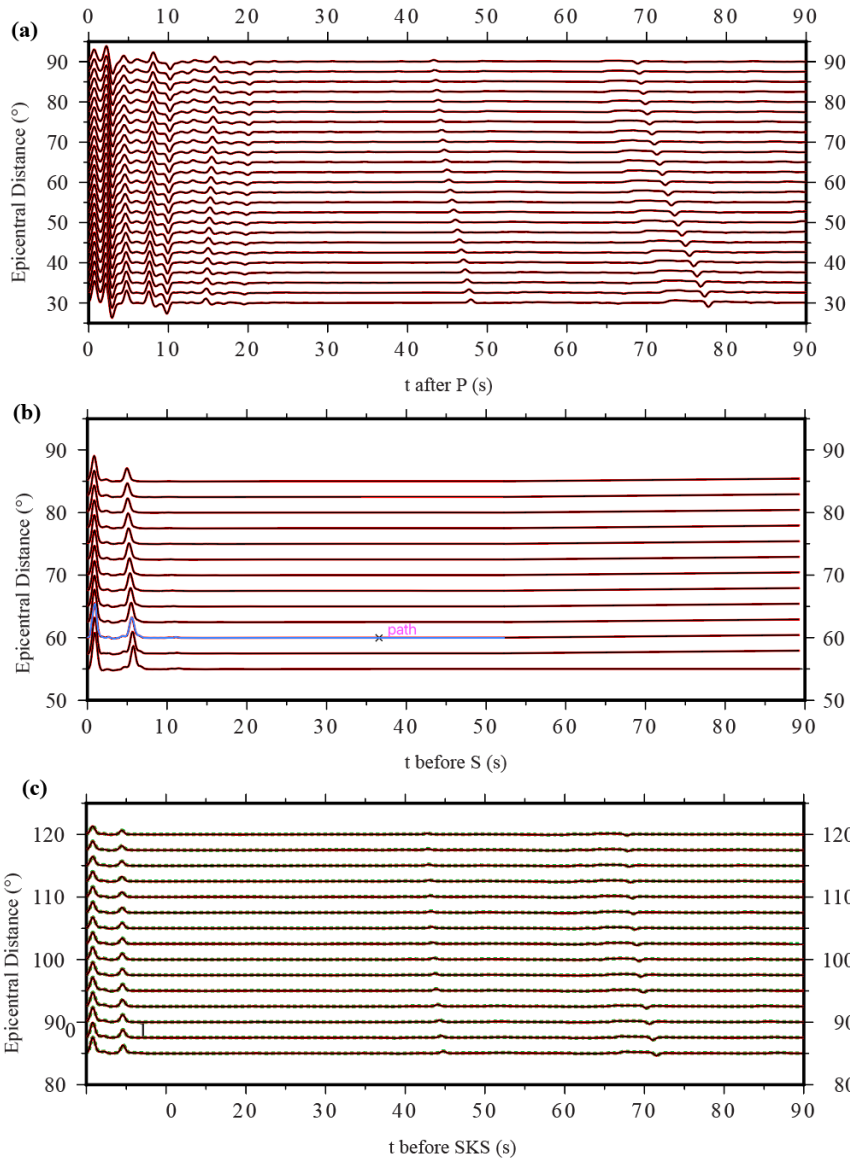
- Formatted: English (US)

438 includes all multiples, transformations, and reflections produced by an arbitrary structure with homogeneous layers
439 (Svenningsen and Jacobsen, 2007). Finally, the Z (or L) component records are deconvolved from the R (or Q)
440 components, and a Gaussian low-pass filter is applied to the resulting seismogram. For the S wave incidence, the resultant
441 seismograms are subject to time and sign reversals, following the convention for S receiver functions (e.g., Yuan et al.,
442 2006). This process is repeated n times (as many RFs are input by the user) for a list of events (epicentral distances and
443 depths). The resulting n receiver functions are stacked via move-out correction considering the IASPI91 model and a
444 reference velocity of 6.4 km/s (e.g., Rondenay, 2009). The final stacked receiver functions are compared with the
445 observed waveforms to measure misfits. Fig. 6 shows a comparison between the results of the RF computations in
446 TCSEIS-1D and those from other codes in order to validate the results.

447 For these comparisons (and by default in the code), RF are normalized, as amplitude values may vary with instruments
448 and processing. No other corrections are applied to the final stack, and the post-processing (if required) is left to the end
449 user. Furthermore, attenuation and anisotropy effects are not accounted for, the code automatically outputs a geophysical
450 model (z , V_p , V_s , ρ , Q_s , γ) that can be used for forward computation and individual RF for post-processing using other
451 modelling tools. It is important to keep in mind that real RF are highly dependent on the quality of the data and the steps
452 used by the interpreter. In general, there are several ways to approach the deconvolution of the horizontal and vertical
453 components of the seismogram that may differ from the scheme presented here (e.g., Pesce, 2010). Here, we use the now-
454 classic implementation of the frequency-domain water-level algorithm (e.g., Langston, 1979; Rondenay, 2009). Hence,
455 when modeling real RF with TCSEIS-1D, care must be taken to consider the aforementioned points for consistency,
456 especially regarding anisotropy and attenuation.

457
458
459
460
461
462
463
464
465
466
467
468
469
470
471

Formatted: English (US)



472
 473 **Figure 6:** Comparison between the synthetic Receiver Functions (RF) computed by the code and those computed with other
 474 codes. (a) P-to-S RF, (b) S-to-P RF and (c) SKS-to-P RF. RF in red correspond to our code, those in black were computed with
 475 the Matlab codes by Bo Holm Jacobsen (2008; Svenningsen and Jacobsen, 2007), and on green those computed in IRFFM2
 476 V1.2 (Tkalčić et al, 2012, only P-to-S available). Difference are small (error < 0.1%). For this example the gaussian parameter
 477 $a = 2.5$ (roughly between 0.4 and 1 Hz).

Formatted: English (US)

478
 479

480 **3. Testing TCSEIS-1D: Sensitivity analysis**

481 To illustrate the capabilities of TCSEIS-1D, we present three simple examples that demonstrate the sensitivity of Rayleigh
482 wave phase velocity curves and P-to-S receiver functions to compositional and temperature variations with respect to a
483 reference model (Figure. 14–16). The reference model in our examples is characterized by:

Formatted: English (US)

- 484
- 485 i. A 40-km-thick crust with a 2-km shale sedimentary layer (Qz(%)=30, Carbo(%)=10, Clays(%)=60, Porosity(%)=5), a
486 20 km thick monzodioritic (felsic) upper crust (Qz(%)=10, K-feldspar(%)=90, Plagioclase(%)=0), and a 20-km thick
487 orthopyroxene-gabbroic (mafic) lower crust (Anorthosite(%)=20, Clinopyroxene(%)=60, Orthopyroxene(%)=20).
- 488 ii. A 200-km-thick lithosphere with a LAB temperature of 1300 °C.
- 489
- 490 iii. A uniform whole mantle composition: Al₂O₃=3.6 wt% and FeO=8.0 wt% (e.g., McDonough and Sun, 1995) with
491 constant grain size (10 mm).
- 492 iv. Isotropic model (i.e., no radial anisotropy)
- 493

Formatted: English (US)

494 **3.1 Example 1: Average Mantle Composition**

495 In this first example (Fig. 7), we change the composition of the entire mantle. The values for the two independent oxides
496 in our parametrization (Al₂O₃ = 3.6 wt% and FeO = 8.0 wt%) correspond to the primitive mantle composition from
497 McDonough and Sun (1995). Here, we explore the effect of changing the value of Al₂O₃ to 2.0 wt% and to 5.0 wt% (for
498 a constant value of FeO wt%). Then, the effect of changing the values of FeO to 6.0% and 10.0% (for a constant value of
499 Al₂O₃ wt%). From this simple test, we can draw a few important conclusions:

Formatted: English (US)

Formatted: English (US)

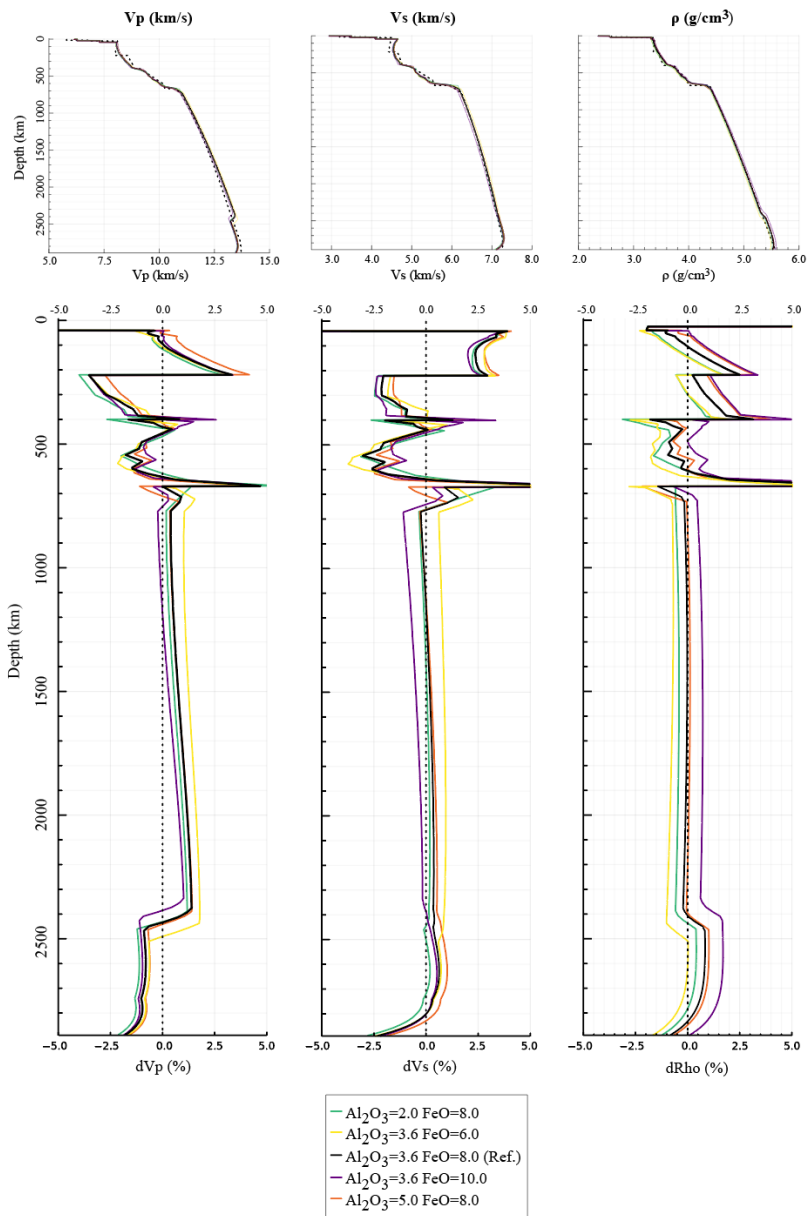
Formatted: English (US)

Formatted: English (US)

- 500 - The amount of Al₂O₃ dominates the velocity gradients in the upper mantle, with velocity variations being proportional
501 to Al₂O₃ content. However, Al₂O₃ has a limited effect on the lower mantle.
- 502 - The amount of FeO dictates the velocity gradients in the lower mantle while having a minor effect in the upper mantle.
- 503 In general terms, velocity gradients are inversely proportional to the wt% of FeO in the lower mantle. Interestingly FeO
504 has a dramatic effect on the gradient at the top of the D'' layer, changing its depth by ~100 km within our test.
- 505 - The sharpness and depth of the transition zone boundaries is controlled by mantle composition. Both Al₂O₃ and FeO
506 appear to have a dramatic effect on the 410 km discontinuity (olivine->wadsleyite) sharpness. By contrast, the 560 km
507 discontinuity (wadsleyite->ringwoodite) and the 660 km discontinuity (ringwoodite+majorite-
508 >perovskite+ferropericlasite) are mostly affected by FeO and Al₂O₃ respectively.

509 We note that within the chemical parametrization in TCSEIS-1D, the amount of CaO and MgO oxides is dependent on
510 the amount of Al₂O₃ based on statistical correlations from global petrological data bases (Afonso et al., 2013a). By
511 contrast, the amount of FeO is an independent variable.

512



513
514
515
516
517
518
519

Figure 7: Example 1. Comparison between the results of a constant composition mantle in TCSEIS-1D (solid lines) and the PREM model (dashed). Here we have tested several compositions to show how large Vp, Vs and Rho anomalies can arise from extreme values of Al₂O₃ and FeO. Top panels show the comparison in absolute Vp, Vs and Rho values, while the bottom panel shows anomalies with respect to PREM. In the bottom panel, crustal anomalies have been deleted from the presentation as they are too large as PREM has a poorly estimated crust.

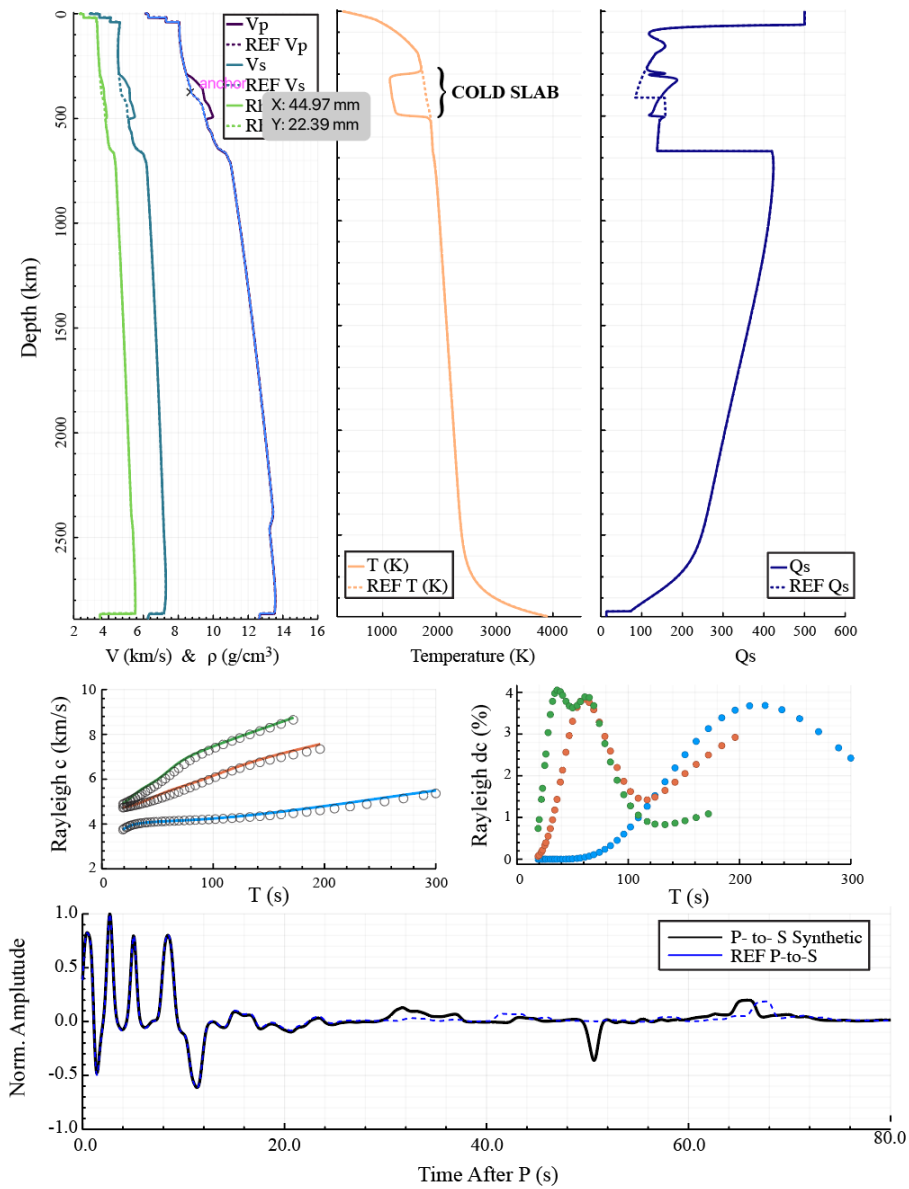
Formatted: English (US)

Formatted: English (US)

520 **3.2 Example 2: Cold horizontally stagnating slab**

521 In the second example (Fig. 8), we implement a thermal and compositional anomaly with respect to the reference model
522 representing a 1D section of a cold horizontally stagnating slab (a subducted slab that changes direction in the transition
523 mantle; e.g., Fukao et al., 2009). The anomaly is defined from 300 km to 500 km depth (Fig. 14) and is characterized by:
524 (a) a -600 K thermal anomaly with respect to the ambient mantle; and (b) a chemical anomaly of $\text{Al}_2\text{O}_3 = -0.25 \text{ wt}\%$ with
525 respect to our reference model. The mantle in the "slab" region shows higher values for velocities, density, and Q_s than
526 the reference model. These positive anomalies are easily recognized in the Rayleigh wave dispersion curves: for the long
527 periods in the fundamental mode and, in general, for the higher dispersion modes, the phase velocity anomalies are >
528 +3%. The P-to-S receiver function is only modified for periods > 20 s (arrival of late phases) due to the upward shift of
529 the 410 km discontinuity caused by the "slab" anomaly.
530

Formatted: English (US)

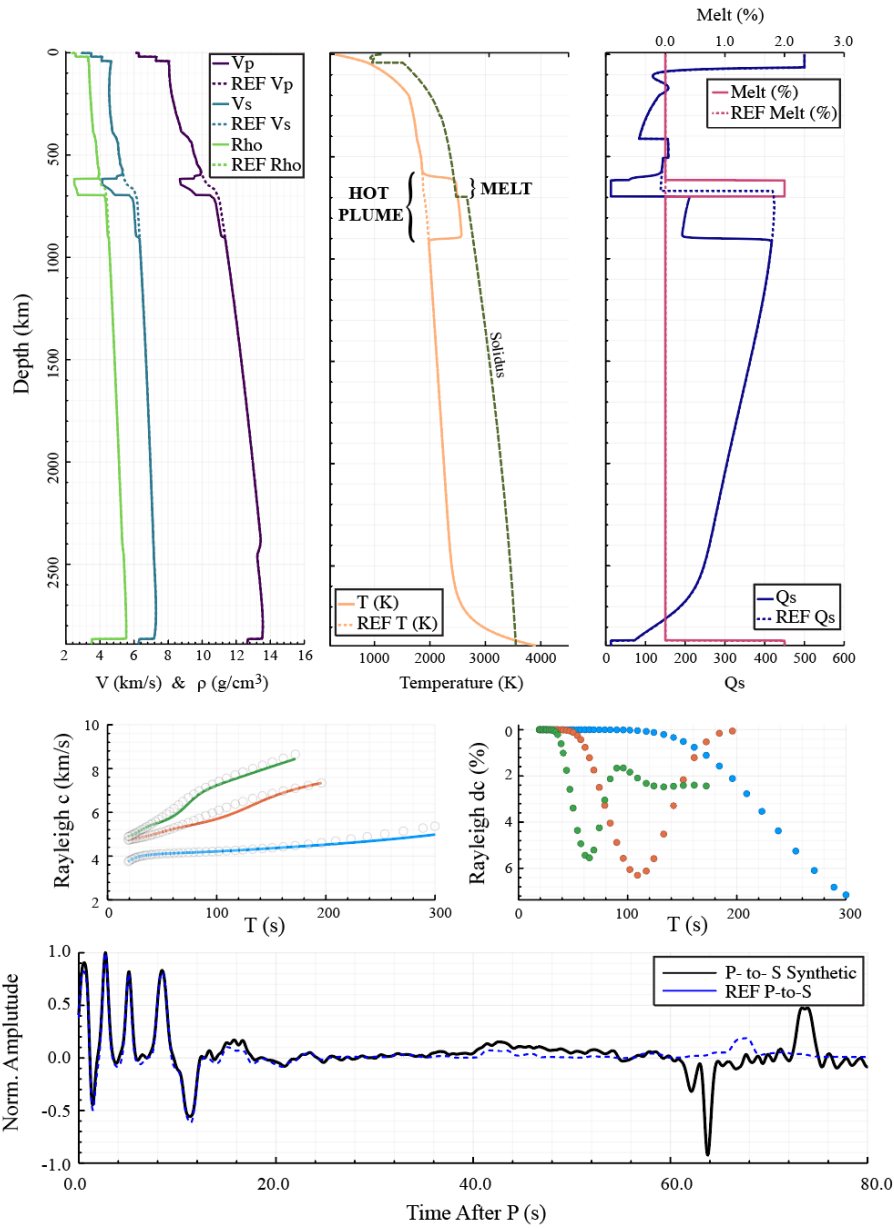


531
 532 Figure 8: Example 2 showing the effect of a cold slab-like feature plunging into the transition zone. On the top: the left panel
 533 shows the V_p , V_s and ρ profiles with depth (solid lines are the computed parameters and dashed ones are the PREM values),
 534 in the center we show the temperature profile with (T) and without (Ref T), and on the right the attenuation profile with (Qs)
 535 and without the slab (Qs Ref). On the centre of the figure we present: on the left the dispersion curves of the model with (solid
 536 lines) and without (circles) the slab for the fundamental mode (blue) and the 1st (orange) and second (green) overtones.
 537 Anomalies between both are presented in the right panel. At the bottom P-to-S RF with (black) and without (blue) are shown.
 538 Notice that, except for the first panel, Ref is the reference model without anomalies (see text for details).

539 **3.3 Example 3: Hot ponding plume head**

540 In the third example (Fig. 9), we implement a thermal and compositional anomaly with respect to the reference model
541 representing a 1D section of a hot horizontally flowing or ponding plume head (wide horizontal zones that extend from
542 the vertical plume conduct at discontinuities; e.g., Dongmo Wamba et al., 2023). The “plume” is the anomaly, which is
543 defined from 600 km to 900 km depth (Fig. 15) and is characterized by: (a) a +600 K thermal anomaly with respect to the
544 ambient mantle; and (b) a chemical anomaly of $\text{Al}_2\text{O}_3 = +0.25 \text{ wt\%}$ and $\text{FeO} = +0.5 \text{ wt\%}$. The “plume” anomaly shows
545 lower values for the velocities, density, and Q_s than the reference model. In this case, the anomalous region is divided
546 into two sections: the upper part (600 km–700 km depth) with extremely low anomalies (caused by melting atop the
547 plume), and the lower part (depth > 700 km) where the decrease in the physical parameters is less pronounced. The
548 temperature and composition anomalies strongly affect synthetic Rayleigh wave dispersion curves. For the long periods
549 in the fundamental mode, and in general for the higher dispersion modes, the phase velocity anomalies are < -5%. The P-
550 to-S receiver function is modified for periods > 40 s as all the lower part of the transition zone is affected by the anomaly,
551 which also generates sharp impedance contrasts. It is worth noting that the effect of the anomaly in this example is so
552 significant that the crustal phases recorded in the receiver functions are slightly affected as well.
553

Formatted: English (US)



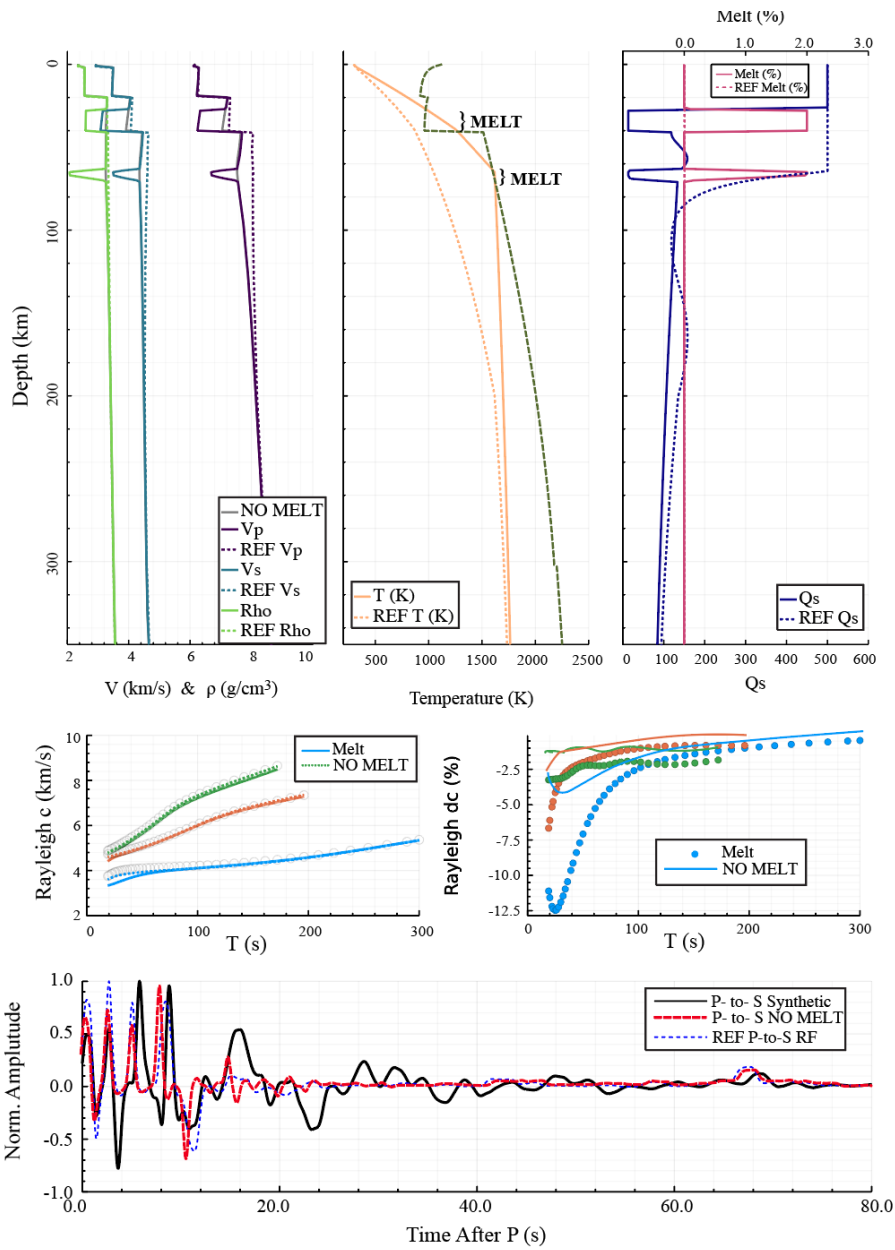
554
555
556
557
558
559

Figure 9: Example 2 showing the effect of a hot plume-like feature entering the transition zone from below. Panels are in the same configuration as in Fig. 8, but in this case we are the melt curve to the top right plot.

Formatted: English (US)

560 **3.3 Example 4: Thin Lithosphere**

561 In the final example, we leave most parameters from the reference model constant and change the base of the lithosphere
562 from 200 km in the reference model to 60 km (Fig. 16). This change has a drastic effect on the model as two melt regions
563 appear, one near the LAB and the other at the base of the crust, causing two low velocity, density, and Qs regions at 35
564 km and 70 km depth, respectively. The effect of the lithospheric thinning is strong in the predicted surface wave dispersion
565 curves, in particular for the fundamental mode, where large negative anomalies are apparent, and less so for the overtones.
566 The waveform of the P-to-S receiver function drastically changes due to the negative impedances present within the crust
567 and upper mantle in our example model. The effect is much less dramatic but still present if the melt modeling option is
568 turned off.



569
570
571
572
573

Fig 10 : Example 3 showing the effect of a thin lithosphere under an average continental crust. Panels are the same as in Fig. 8. Here we show two outputs: with melt (MELT, same as in previous examples) and without melt (NO MELT, dotted lines).

Formatted: English (US)

574
575
576
577
578
579
580
581
582
583
584
585
586
587
588
589
590
591
592
593
594
595
596
597
598
599
600
601
602
603
604
605
606
607
608
609
610
611
612
613
614

4. Remarks, conclusions and further work

Receiver functions and surface wave dispersion data analysis has led to remarkable results revealing the Earth's internal structure in terms of compressional and shear waves velocity anomalies (δV_p , δV_s). Yet, the interpretation of these anomalies in terms of crustal and mantle composition is a challenging modelling task. The usage of these data under geophysical-petrological schemes have proven to yield important results in terms of the thermal and petrological structure of the Earth's mantle (e.g. Munch et al., 2018; Bissig et al., 2021; Afonso et al., 2022; Fullea et al., 2021; Munch et al., 2021; Lebedev et al., 2024). Yet, the usage of this type of methods is not common.

In order to build a bridge to go from classical seismological approaches to the thermal-petrological realm, we present TCSEIS-1D, a new, open-source, cross-platform, easy-to-use, and accurate code to model the crust and whole mantle using surface wave dispersion curves (including group and phase velocity of Rayleigh and Love waves for the fundamental mode, as well as several overtones) and three widely used receiver functions (P-to-S, S-to-P, and SKS-to-P) directly in terms of rock composition and the in-situ temperature and pressure conditions. We achieved this by creating an interface between the modeling of seismic data and mineral/phase equilibria calculations that allow for the calculation of elastic properties (i.e., V_p , V_s , and density) as a function of temperature, pressure, and composition. Moreover, TCSEIS-1D can be used as a simple geophysical model (i.e., seismic velocities and density) generator based on input thermochemical conditions that can be coupled to third-party seismic codes to perform forward calculations, offering as well a variety of tools intended to interpret geophysical data and models in petrological (e.g., property maps in the TPC space; Fig. 1) and geodynamical terms (e.g. different thermal scenarios, Figs. 14-16).

TCSEIS-1D can be used to simultaneously fit different real seismological and other geophysical data sets within a trial-and-error approach or to carry out synthetic modeling (e.g., sensitivity analysis), making it a useful tool for a wide range of geoscientists. Future work includes developing an inversion scheme of seismic data for the thermochemical structure of the crust and mantle based on TCSEIS-1D.

615
616
617

618 **Appendix A: TCSEIS-1D Surface Wave Dispersion native package: SWD.jl**

619 SWD.jl is mostly based in the formulation described by Haney and Tsai (2015, 2017, 2019). These authors utilize (for
620 both Rayleigh and Love waves) a finite element approach based on the thin-layer method (Lysmer, 1970; Kausel, 2005).
621 In contrast to the popular Thomson-Haskell recursion formula (e.g., Takeuchi and Saito, 1972; Saito, 1988), Haney and
622 Tsai employed several thin layers leading to a generalized eigenvalue/eigenvector problem that must be solved for every
623 sampled frequency ($1/T_{\text{Observed}}$, Hz). Their method is both accurate and fast and allows for the consideration of a water
624 layer on top of the model column. However, as originally proposed, the method is hampered by two shortcomings: (1) it
625 assumes the Earth is isotropic, elastic and flat, and (2) it requires the specification of a relatively dense Finite Elements
626 (FEM) mesh. We address each one of these as follows:

627

628 (a) We decouple the computation of Rayleigh and Love waves based on the vertically and horizontally polarized
629 $V_s(\mathcal{JPC})$ components, V_{SV} and V_{SH} , respectively defined as:

630
$$V_{SV} = (1 - \frac{1}{3}\chi)V_s \text{ (Eq. A.1)}$$

631
$$V_{SH} = (\frac{2}{3}\chi + 1)V_s \text{ (Eq. A.2)}$$

632 Where χ is the average seismic radial anisotropy for each layer (user input). Rayleigh and Love dispersion curves
633 are computed as a function of V_{SV} and V_{SH} respectively.

634

635 We include anelastic effects as stated by Karato, (1993), Minster and Anderson (1981), Afonso et al. (2005), Fullea et al.
636 (2021), via the expressions:

637
$$V_{Pa} = V_p(1 - \frac{2}{9}\cot(\frac{\pi\alpha}{2})Q_s^{-1}) \text{ (Eq. A.3)}$$

638
$$V_{Sa} = V_s(1 - \frac{1}{2}\cot(\frac{\pi\alpha}{2})Q_s^{-1}) \text{ (Eq. A.4)}$$

639 Where, V_{Pa} and V_{Sa} are the anelastic P and S velocities, and V_p and V_s are the anharmonic velocities computed from
640 \mathcal{JPC} values. Further details on estimating Q_s are presented in section 2.6.

641 (b) We consider the Earth's sphericity correcting the values of V_p , V_s and ρ for the Earth-flattening approximation
642 before computing the dispersion curves. Here, we follow Herrmann (2013) for Rayleigh waves, and the equations
643 by Schwab and Knopoff (1972) for Love waves. The depth from the surface in the equivalent flat Earth model,
644 z , is given by:

645
$$z = a \ln \frac{a}{r} \text{ (Eq. A.5)}$$

646 Where r is the radial distance from the center of the Earth, and a is the Earth's radius. Hence, if we consider a
647 spherical layer bounded by r_i and r_{i-1} radii, with $r_{i-1} > r_i$, then the thickness, h , of the corresponding i^{th} flat layer is
648 given by:

649
$$(h_i)_f = a \ln(\frac{a}{r_i}) - a \ln(\frac{a}{r_{i-1}}) \text{ (Eq. A.6)}$$

650 The mean V_p , V_s and ρ in the transformed flat layer model, $(V_{pi})_f$, $(V_{si})_f$, $(\rho_i)_f$ and are given by

651
$$(V_{pi})_f = (V_{pi})_s \frac{2a}{r_i + r_{i-1}} \text{ (Eq. A.7)}$$

652
$$(V_{si})_f = (V_{si})_s \frac{2a}{r_i + r_{i-1}} \text{ (Eq. A.8)}$$

653
654
655
656
657
658
659
660
661
662
663
664
665
666
667
668
669
670
671
672
673
674
675
676
677
678
679
680
681
682
683
684
685
686
687
688
689
690
691
692

$$(\rho_i)_f = (\rho_i)_s \left(\frac{z a}{r_i + r_{i-1}} \right)^{SE} \quad (\text{Eq. A.9})$$

Where $(V_p)_s$, $(V_s)_s$, $(\rho)_s$ are the mean V_p , V_s and ρ in the spherical model, and SE is a parameter that takes a different value for Love ($SE=-5$, Schwab and Knopoff, 1972) and Rayleigh (we find a better fit with an exponent value of $SE=-2.278$ instead of $SE=-2.275$ as originally reported in Herrmann (2013)).

- (c) Finally, we optimize the FEM mesh for the forward computation (e.g., Xia et al., 1999, Ma and Clayton, 2016, Hanney and Tsai, 2015, 2017, 2019). Generally, the required mesh must have adequate sampling above the sensitivity depth of each period, without oversampling the model below it unnecessarily. As a rule of thumb, more than five 5 layers (6 nodes) are required in the sensitivity depths of each frequency with their thicknesses increasing exponentially from the surface to the bottom of the model (e.g., Hanney and Tsai, 2017). In TCSEIS-1D, the user has two possibilities: (i) using a precomputed mesh (the Golden Mesh) created with smaller layers than those required to compute the dispersion at any period between 1 s and 500 s, and slightly oversampling the base of the model; or (ii) using a new mesh based on the lowest period of the input data and a low threshold of Rayleigh wave phase velocity set to 1 km/s (see Hanney and Tsai, 2017, Appendix D for more details). Our mesh samples all the space, and the thickness of each layer coincides with the sensitivity of both Rayleigh waves and Love waves (depending on the period). Our FEM grids for surface waves are designed to compute dispersion curves in the period range from 5 s to 500 s.

693
694
695
696
697
698
699
700
701
702
703
704
705
706
707
708
709
710
711
712
713
714
715
716
717
718
719
720
721
722
723
724
725
726
727
728

Appendix B: seismic attenuation model

Dannberg et al (2017) pose that the response of a continuum that behaves according to Burgers model of linear viscoelasticity with creep function in response to a sinusoidally time-varying stress (e.g., a dispersive wave) is given by the dynamic compliance $J^*(\omega)$ (the Laplace transform of its creep function). This function takes the form:

$$J^*(\omega) = J_1(\omega) + iJ_2(\omega) \text{ (Eq. B1)}$$

$$J_1 = J_u \left\{ 1 + \frac{\alpha \Delta_B}{\tau_H^\alpha - \tau_L^\alpha} \int_{\tau_L}^{\tau_H} \frac{\tau^{\alpha-1}}{1+\omega^2\tau^2} d\tau + \frac{\Delta_P}{\sigma\sqrt{2\pi}} \int_0^\infty \frac{1}{\tau(1+\omega^2\tau^2)} \exp\left(-\frac{\ln(\frac{\tau}{\tau_P})^2}{2\sigma^2}\right) d\tau \right\} \text{ (Eq. B2)}$$

$$J_2 = J_u \left\{ \frac{\omega \alpha \Delta_B}{\tau_H^\alpha - \tau_L^\alpha} \int_{\tau_L}^{\tau_H} \frac{\tau^\alpha}{1+\omega^2\tau^2} d\tau + \frac{\omega \Delta_P}{\sigma\sqrt{2\pi}} \int_0^\infty \frac{1}{1+\omega^2\tau^2} \exp\left(-\frac{\ln(\frac{\tau}{\tau_P})^2}{2\sigma^2}\right) d\tau + \frac{1}{\omega\tau_M} \right\} \text{ (Eq. B3)}$$

Where ω is the angular frequency, $\omega = 2\pi/T$, α is the anelastic frequency exponent, Δ_B is the Burgers element strength and Δ_P and σ are the peak height and width, and J_u is the unrelaxed compliance (which is not computed for Q_s estimations).

All the timescales τ_i control the temperature, pressure, and grain size sensitivity of the anelastic scaling relationships:

$$\tau_i = \tau_{iR} \left(\frac{d}{d_R}\right)^{m_i} \exp \left[\left(\frac{E^*}{R}\right) \left(\frac{1}{T} - \frac{1}{T_R}\right) + \left(\frac{V^*}{R}\right) \left(\frac{P}{T} - \frac{P_R}{T_R}\right) \right] \text{ (Eq. B4)}$$

where $i = H, L, P, M$ are the upper, lower, peak and Maxwell viscous relaxation values respectively, and all m_j are grain size exponents with $j=H, L, P$ for anelastic relaxation (m_a), and $j=M$ for viscous relaxation (m_v). Here, E^* and V^* are the activation energy and volume for the anelastic model. We use the same values for each major mantle zone as reported in the supplementary material of Dannberg et al. (2017). The temperature, pressure, and grain size sensitivity of the anelastic relationships are introduced in terms of reference values T_R, P_R and d_R .

$$Q_s = \frac{J_1(\omega)}{J_2(\omega)} \text{ (Eq. B5)}$$

and

$$Q_p = \frac{9}{4} Q_s \text{ (Eq. B 6)}$$

which implicates an infinite quality factor for the bulk modulus (e.g., Karato, 1993; Minster and Anderson, 1981).

Formatted: English (US)

729 **Acknowledgements**

730

731 MA was funded by Comunidad Autonoma de Madrid (Spain) through an “Atracción de Talento” senior fellowship (2018-
732 T1/AMB/11493) to JF, who is also supported the Spanish Ministry of Science and Innovation (PID2020-114854GB-C22
733 and CNS2022-135621).

734 **Data Availability Statement**

735 The full TCSEIS-ID v1.0 package is openly available for download at the project’s GitHub repository
736 (<https://github.com/marianoarnaiz/TCSEIS>). The software requires a functional installation of the Julia Language
737 (version 1.7 or higher) to run

738

739 **Author contribution statement:**

740

741 MA and JF co-designed the algorithms, and co-wrote the manuscript. MA wrote the code in Julia language. JF supervised
742 the research project and tested the code.

743

744

745

746

747

748

749

750

751

752

753

754

755

756

757

758

759

760

761

762

763

764

765

766

767

768

769

770

771

772

773

- 774 **References**
- 775 Abers, G. A. and Hacker, B. R.: A MATLAB toolbox and Excel workbook for calculating the densities, seismic wave
776 speeds, and major element composition of minerals and rocks at pressure and temperature, *Geochem. Geophys.*
777 *Geosyst.*, 16, 616–624, <https://doi.org/10.1002/2015GC006091>, 2016.
- 778 Afonso, J. C., Ranalli, G., and Fernández, M.: Thermal expansivity and elastic properties of the lithospheric mantle:
779 results from mineral physics of composites, *Phys. Earth Planet. Int.*, 149, 279–306,
780 <https://doi.org/10.1016/j.pepi.2004.09.008>, 2005.
- 781 Aki, K., Christoffersson, A., and Husebye, E. S.: Determination of the 3-dimensional seismic structure of the
782 lithosphere, *J. Geophys. Res.*, 82, 277–296, <https://doi.org/10.1029/JB082i002p00277>, 1977.
- 783 Andrault, D., Pesce, G., Manthilake, G., Monteux, J., Bolfan-Casanova, N., Chantel, J., Novella, D., Guignot, N., King,
784 A., Itié, J.-P., and Hennet, L.: Deep and persistent melt layer in the Archaean mantle, *Nat. Geosci.*, 11, 139–143,
785 <https://doi.org/10.1038/s41561-017-0053-9>, 2018.
- 786 Arnaiz-Rodríguez, M. S., Zhao, Y., Sánchez-Gamboa, A. K., and Audemard, F.: Crustal and upper-mantle structure of
787 the Eastern Caribbean and Northern Venezuela from passive Rayleigh wave tomography, *Tectonophysics*, 804, 228711,
788 <https://doi.org/10.1016/j.tecto.2020.228711>, 2020.
- 789 Athy, L. F.: Density, porosity and compaction of sedimentary rocks, *AAPG Bull.*, 14, 1–24,
790 <https://doi.org/10.1306/3D9322C5-16B1-11D7-8645000102C1865D>, 1930.
- 791 Audkhkhasi, P. and Singh, S. C.: Discovery of distinct lithosphere-asthenosphere boundary and the Gutenberg
792 discontinuity in the Atlantic Ocean, *Sci. Adv.*, 8, eabn5404, <https://doi.org/10.1126/sciadv.abn5404>, 2022.
- 793 Ball, P. W., White, N. J., MacLennan, J., et al.: Global influence of mantle temperature and plate thickness on intraplate
794 volcanism, *Nat. Commun.*, 12, 2045, <https://doi.org/10.1038/s41467-021-22323-9>, 2021.
- 795 Bezanson, J., Edelman, A., Karpinski, S., and Shah, V. B.: Julia: A Fresh Approach to Numerical Computing, *SIAM*
796 *Rev.*, 59, 65–98, <https://doi.org/10.1137/141000671>, 2017.
- 797 Bissell, H. J., Haaf, E. T., Crook, K. A. W., Beck, K. C., Schwab, F. L., and Folk, R. L.: Sedimentary rocks,
798 *Encyclopædia Britannica*, <https://www.britannica.com/science/sedimentary-rock>, accessed 9 Dec 2021.
- 799 Bissig, F., Khan, A., Tauzin, B., Sossi, P. A., Münch, F. D., and Giardini, D.: Multifrequency inversion of Ps and Sp
800 receiver functions: methodology and application to USArray data, *J. Geophys. Res. Solid Earth*, 126, e2020JB020350,
801 <https://doi.org/10.1029/2020JB020350>, 2021.
- 802 Bosch, M.: Lithologic tomography: from plural geophysical data to lithology estimation, *J. Geophys. Res.*, 104, 749–
803 766, <https://doi.org/10.1029/1998JB900035>, 1999.
- 804 Boujibar, A., Bolfan-Casanova, N., Andrault, D., Bouhifd, M. A., and Trcera, N.: Incorporation of Fe²⁺ and Fe³⁺ in
805 bridgmanite during magma ocean crystallization, *Am. Mineral.*, 101, 1560–1570, <https://doi.org/10.2138/am-2016-5561>, 2016.
- 806

Formatted: English (US)

Formatted: Font: Bold, Text Outline

807 Brocher, T. M.: Empirical relations between elastic wavespeeds and density in the Earth's crust, *Bull. Seismol. Soc.*
808 *Am.*, 95, 2081–2092, <https://doi.org/10.1785/0120040090>, 2005.

809 Calò, M., Bodin, T., and Romanowicz, B.: Layered structure in the upper mantle across North America from joint
810 inversion of long and short period seismic data, *Earth Planet. Sci. Lett.*, 449, 164–175,
811 <https://doi.org/10.1016/j.epsl.2016.05.054>, 2016.

812 Chen, X., Park, J., and Levin, V.: Anisotropic layering and seismic body waves: deformation gradients, initial
813 S-polarizations, and converted-wave birefringence, *Pure Appl. Geophys.*, 178, 2001–2023,
814 <https://doi.org/10.1007/s00024-021-02755-6>, 2021.

815 Connolly, J. A. D.: Computation of phase equilibria by linear programming: a tool for geodynamic modeling and its
816 application to subduction zone decarbonation, *Earth Planet. Sci. Lett.*, 236, 524–541,
817 <https://doi.org/10.1016/j.epsl.2005.03.039>, 2005.

818 Connolly, J. A. D.: The geodynamic equation of state: What and how, *Geochem. Geophys. Geosyst.*, 10, Q10014,
819 <https://doi.org/10.1029/2009GC002540>, 2009.

820 Dinari, O., Yu, A., Freifeld, O., and Fisher, J.: Distributed MCMC inference in Dirichlet process mixture models using
821 Julia, in *Proc. IEEE/ACM CCGrid*, 518–525, <https://doi.org/10.1109/CCGRID.2019.00066>, 2019.

822 Dongmo Wamba, M., Montagner, J.-P., and Romanowicz, B.: Imaging deep-mantle plumbing beneath La Réunion and
823 Comores hot spots: vertical plume conduits and horizontal ponding zones, *Sci. Adv.*, 9, eade3723,
824 <https://doi.org/10.1126/sciadv.ade3723>, 2023.

825 Faul, U. H. and Jackson, I.: The seismological signature of temperature and grain size variations in the upper mantle,
826 *Earth Planet. Sci. Lett.*, 234, 119–134, <https://doi.org/10.1016/j.epsl.2005.02.030>, 2005.

827 Fullea, J., Afonso, J. C., Connolly, J. A. D., Fernández, M., Garcia-Castellanos, D., and Zeyen, H.: LitMod3D: an
828 interactive 3-D software to model the thermal, compositional, density, seismological, and rheological structure of the
829 lithosphere and sublithospheric upper mantle, *Geochem. Geophys. Geosyst.*, 10, Q08019,
830 <https://doi.org/10.1029/2009GC002391>, 2009.

831 Fullea, J., Lebedev, S., Martinec, Z., and Celli, N. L.: WINTERC-G: mapping the upper mantle thermochemical
832 heterogeneity from coupled geophysical–petrological inversion of seismic waveforms, heat flow, surface elevation and
833 gravity satellite data, *Geophys. J. Int.*, 226, 146–191, <https://doi.org/10.1093/gji/ggab094>, 2021.

834 Fukao, Y., Obayashi, M., and Nakakuki, T.: Stagnant slab: a review, *Annu. Rev. Earth Planet. Sci.*, 37, 19–46,
835 <https://doi.org/10.1146/annurev.earth.36.031207.124224>, 2009.

836 Gao, K., Mei, G., Piccialli, F., Cuomo, S., Tu, J., and Huo, Z.: Julia language in machine learning: algorithms,
837 applications, and open issues, *Comput. Sci. Rev.*, 37, 100254, <https://doi.org/10.1016/j.cosrev.2020.100254>, 2020.

838 Gerya, T.: *Introduction to Numerical Geodynamic Modelling*, Cambridge University Press, Cambridge, pp. 345,
839 <https://doi.org/10.1017/CBO9780511809101>, 2009.

840 Grand, S. P.: Mantle shear-wave tomography and the fate of subducted slabs, *Philos. Trans. R. Soc. Lond. A*, 360,
841 2475–2491, <https://doi.org/10.1098/rsta.2002.1023>, 2002.

842 Grose, C. J. and Afonso, J. C.: Chemical disequilibria, lithospheric thickness, and the source of ocean island basalts, *J.*
843 *Petrol.*, 60, 755–790, <https://doi.org/10.1093/petrology/egz012>, 2019.

844 Hacker, B. R. and Abers, G. A.: Subduction Factory 3: an Excel worksheet and macro for calculating the densities,
845 seismic wave speeds, and H₂O contents of minerals and rocks at pressure and temperature, *Geochem. Geophys.*
846 *Geosyst.*, 5, Q01005, <https://doi.org/10.1029/2003GC000649>, 2004.

847 Hamblin, W. K. and Christiansen, E. H.: *Earth's dynamic systems*, 10th edn., Prentice Hall, Upper Saddle River, NJ,
848 790 pp., 2004.

849 Haney, M. M. and Tsai, V. C.: Nonperturbational surface-wave inversion: a Dix-type relation for surface waves,
850 *Geophysics*, 80, EN167–EN177, <https://doi.org/10.1190/geo2014-0208.1>, 2015.

851 Haney, M. M. and Tsai, V. C.: Perturbational and nonperturbational inversion of Rayleigh-wave velocities, *Geophysics*,
852 82, F15–F28, <https://doi.org/10.1190/GEO2016-0542.1>, 2017.

853 Haney, M. M. and Tsai, V. C.: Perturbational and nonperturbational inversion of Love-wave velocities, *Geophysics*, 85,
854 F19–F26, <https://doi.org/10.1190/geo2019-0058.1>, 2019.

855 Haskell, N. A.: The dispersion of surface waves on multilayered media, *Bull. Seismol. Soc. Am.*, 43, 17–34, 1953.

856 Herrmann, R. B.: Computer programs in seismology: an evolving tool for instruction and research, *Seism. Res. Lett.*,
857 84, 1081–1088, <https://doi.org/10.1785/0220110096>, 2013.

858 Hofmeister, A. M.: Mantle values of thermal conductivity and the geotherm from phonon lifetimes, *Science*, 283, 1699–
859 1706, <https://doi.org/10.1126/science.283.5409.1699>, 1999.

860 Irifune, T. and Tsuchiya, T.: Phase transitions and mineralogy of the lower mantle, in *Treatise on Geophysics*, Elsevier,
861 pp. 33–60, <https://doi.org/10.1016/B978-0-444-53802-4.00030-0>, 2015.

862 Irifune, T.: Composition and structure of the Earth's mantle: a view from recent high-pressure mineral physics studies,
863 *J. Mineral. Soc. Japan*, 19, 233–243, 1990.

864 Jackson, I., Fitz Gerald, J. D., Faul, U. H., and Tan, B. H.: Grain-size-sensitive seismic wave attenuation in
865 polycrystalline olivine, *J. Geophys. Res.*, 107, 2360, <https://doi.org/10.1029/2001JB001225>, 2002.

866 Julià, J., Ammon, C. J., Herrmann, R. B., and Correig, A. M.: Joint inversion of receiver function and surface wave
867 dispersion observations, *Geophys. J. Int.*, 143, 99–112, <https://doi.org/10.1046/j.1365-246X.2000.00217.x>, 2000.

868 Karato, S.-i. and Wu, P.: Rheology of the upper mantle: a synthesis, *Science*, 260, 771–778,
869 <https://doi.org/10.1126/science.260.5109.771>, 1993.

870 Kausel, E. Some wave propagation modes from simple systems to layered soils, in Lai, C. G., and Wilmanski, K. (eds.),
871 *Surface waves in geomechanics: direct and inverse modeling for soil and rocks*, Springer-Verlag, 165–202, 2005.

872 Kennett, B. L. N.: Seismic wave propagation in stratified media, ANU Press, <https://doi.org/10.2307/j.ctt24h2zr>, 2009.

873 Kennett, B. L. N. and Engdahl, E. R.: Travel times for global earthquake location and phase association, *Geophys. J.*
874 *Int.*, 105, 429–465, <https://doi.org/10.1111/j.1365-246X.1991.tb06724.x>, 1991.

875 Haney, M. M. and Tsai, V. C.: Perturbational and nonperturbational inversion of Love-wave velocities, *Geophysics*, 85,
876 F19–F26, <https://doi.org/10.1190/geo2019-0164.1>, 2020.

877 Huang, Z., Zhao, D., and Wang, L.: Seismic heterogeneity and mantle dynamics of the western Pacific subduction zone,
878 *J. Geophys. Res. Solid Earth*, 116, B10303, <https://doi.org/10.1029/2011JB008401>, 2011.

879 Irifune, T., Isshiki, M., and Katayama, Y.: Iron partitioning and density changes of pyrolite in Earth's lower mantle,
880 *Science*, 292, 1171–1173, <https://doi.org/10.1126/science.1057647>, 2001.

881 Jackson, I. and Faul, U. H.: Grainsize-sensitive viscoelastic relaxation in olivine: towards a robust laboratory-based
882 model for seismological application, *Phys. Earth Planet. Int.*, 183, 151–163, <https://doi.org/10.1016/j.pepi.2010.09.005>,
883 2010.

884 Jackson, M. G. and Dasgupta, R.: Compositional constraints on melting of Earth's heterogeneous mantle and
885 implications for the generation of ocean island basalts, *Rev. Geophys.*, 56, 3–49,
886 <https://doi.org/10.1002/2017RG000558>, 2018.

887 Karato, S.: On the origin of the asthenosphere, *Earth Planet. Sci. Lett.*, 321–322, 95–103,
888 <https://doi.org/10.1016/j.epsl.2012.01.001>, 2012.

889 Kellogg, L. H., Hager, B. H., and van der Hilst, R. D.: Compositional stratification in the deep mantle, *Science*, 283,
890 1881–1884, <https://doi.org/10.1126/science.283.5409.1881>, 1999.

891 Khan, A., Maclennan, J., and Connolly, J. A. D.: Inversion of seismic and geodetic data for the major element chemistry
892 and temperature of the Earth's mantle, *Earth Planet. Sci. Lett.*, 284, 554–568,
893 <https://doi.org/10.1016/j.epsl.2009.05.014>, 2009.

894 Khan, A., Cammarano, F., and Connolly, J. A. D.: Geophysical evidence for melt in the deep mantle, *Nature*, 455, 978–
895 981, <https://doi.org/10.1038/nature07364>, 2008.

896 Kustowski, B., Ekström, G., and Dziewoński, A. M.: Anisotropic shear-wave velocity structure of the Earth's mantle: a
897 global model, *J. Geophys. Res.*, 113, B06306, <https://doi.org/10.1029/2007JB005169>, 2008.

898 Lebedev, S. and van der Hilst, R. D.: Global upper-mantle tomography with the automated multimode inversion of
899 surface and S-wave forms, *Geophys. J. Int.*, 173, 505–518, <https://doi.org/10.1111/j.1365-246X.2008.03721.x>, 2008.

Formatted: French

900 Lekic, V., Cottaar, S., Dziewoński, A., and Romanowicz, B.: Cluster analysis of global lower mantle tomography: a
901 new class of structure and implications for chemical heterogeneity, *Earth Planet. Sci. Lett.*, 357–358, 68–77,
902 <https://doi.org/10.1016/j.epsl.2012.09.014>, 2012.

903 Matas, J., Bass, J. D., Ricard, Y., Mattern, E., and Bukowski, M. S. T.: On the bulk composition of the lower mantle:
904 predictions and limitations from generalized inversion of radial seismic profiles, *Geophys. J. Int.*, 160, 973–990,
905 <https://doi.org/10.1111/j.1365-246X.2005.02526.x>, 2005.

906 Montagner, J. P. and Kennett, B. L. N.: How to reconcile body-wave and normal-mode reference Earth models,
907 *Geophys. J. Int.*, 125, 229–248, <https://doi.org/10.1111/j.1365-246X.1996.tb06548.x>, 1996.

908 Murakami, M., Hirose, K., Kawamura, K., Sata, N., and Ohishi, Y.: Post-perovskite phase transition in MgSiO₃,
909 *Science*, 304, 855–858, <https://doi.org/10.1126/science.1095932>, 2004.

910 Nolet, G., Montelli, R., Dahlen, F. A., Masters, G., Engdahl, E. R., and Hung, S. H.: Seismic evidence for a deep mantle
911 thermal anomaly in the mantle beneath East Africa, *Geophys. Res. Lett.*, 31, L20607,
912 <https://doi.org/10.1029/2004GL020572>, 2004.

913 Ritsema, J., Deuss, A., van Heijst, H. J., and Woodhouse, J. H.: S40RTS: a degree-40 shear-velocity model for the
914 mantle from new Rayleigh wave dispersion, teleseismic traveltime and normal-mode splitting function measurements,
915 *Geophys. J. Int.*, 184, 1223–1236, <https://doi.org/10.1111/j.1365-246X.2010.04884.x>, 2011.

916 Rudolph, M. L., Lekic, V., and Lithgow-Bertelloni, C.: Viscosity jump in Earth's mid-mantle, *Science*, 350, 1349–
917 1352, <https://doi.org/10.1126/science.aad1929>, 2015.

918 Simmons, N. A., Forte, A. M., and Grand, S. P.: Thermochemical structure and dynamics of the African superplume,
919 *Geophys. Res. Lett.*, 34, L02301, <https://doi.org/10.1029/2006GL028009>, 2007.

920 Stixrude, L. and Lithgow-Bertelloni, C.: Thermodynamics of mantle minerals – I. Physical properties, *Geophys. J. Int.*,
921 162, 610–632, <https://doi.org/10.1111/j.1365-246X.2005.02642.x>, 2005.

922 Stixrude, L. and Lithgow-Bertelloni, C.: Thermodynamics of mantle minerals – II. Phase equilibria, *Geophys. J. Int.*,
923 184, 1180–1213, <https://doi.org/10.1111/j.1365-246X.2010.04890.x>, 2011.

924 Takei, Y.: Effect of pore geometry on Vp/Vs: From equilibrium geometry to crack, *J. Geophys. Res. Solid Earth*, 107,
925 ECV 6-1–ECV 6-12, <https://doi.org/10.1029/2001JB000522>, 2002.

926 Tsuchiya, T., Tsuchiya, J., Umemoto, K., and Wentzcovitch, R. M.: Phase transition in MgSiO₃ perovskite in the
927 Earth's lower mantle, *Earth Planet. Sci. Lett.*, 224, 241–248, <https://doi.org/10.1016/j.epsl.2004.05.017>, 2004.

928 van der Hilst, R. D., Widiyantoro, S., and Engdahl, E. R.: Evidence for deep mantle circulation from global
929 tomography, *Nature*, 386, 578–584, <https://doi.org/10.1038/386578a0>, 1997.

930 Walter, M. J., Kohn, S. C., Araujo, D., Bulanova, G. P., Smith, C. B., Gaillou, E., Wang, J., Steele, A., and Shirey, S. B.:
931 Deep mantle cycling of oceanic crust: evidence from diamonds and their mineral inclusions, *Science*, 334, 54–57,
932 <https://doi.org/10.1126/science.1209300>, 2011.